*J. Fluid Mech.* (1990), *vol.* 220, *pp.* 1–52
*Printed in Great Britain*



# Homogeneous turbulence in the presence of rotation

By L. JACQUIN[1], O. LEUCHTER[1], C. CAMBON[2] AND J. MATHIEU[2]

[1] Office National d'Etudes et de Recherches Aerospatiales (ONERA) Châtillon, France

[2] Laboratoire de Mécanique des Fluides, Ecole Centrale de Lyon Ecully, France

(Received 13 September 1989)

Turbulence in solid-body rotation is generated by a flow of air passing through a rotating cylinder containing a dense honeycomb structure and a turbulence-producing grid. The velocity field is probed downstream of this device by hot-wire probes. Using the statistical quantities characterizing the fluctuating field, we show that the rotation affects mainly the components normal to the rotation axis and that these effects are triggered when the Rossby numbers constructed from macroscopic turbulent quantities, are less than unity. These results are discussed in the framework of other available experimental results on the subject. A theoretical interpretation, chiefly based on spectral analysis, is then proposed to explain the trends of the observations.

## 1. Introduction

The effects of rotation on turbulence concern all domains of fluid dynamics. However, in typical natural or industrial situations, rotation is often coupled with other dynamical factors such as deformation (shear flows), buoyancy (atmospheric and oceanic motion), or combustion (propulsion).

In view of these various and complex situations, there is much to be gained by understanding the specific role of rotation in the absence of any other external mechanisms. For this, we consider the ideal case of a homogeneous rotating turbulence in an isothermal, incompressible fluid. If the mean velocity field corresponds to a strict solid-body rotation, statistical homogeneity of the fluctuating field is preserved and rotation acts as an external body force.

This problem enters into the classical framework of anisotropic homogeneous turbulence, where the object is to know how the turbulent field reacts to the distortion associated with a particular mean flow. To preserve the homogeneity of the fluctuations, the mean flows are restricted to pure strain, solid-body rotation or a combination of these. Shear, which is a superposition of rotation and plane deformation, of equal rates, is in the latter class of flow.

In a strained as well as in a sheared homogeneous turbulence the linear effects associated with the deformation dominate the dynamics of the flow, at least in a first phase, and the nonlinearity has to be modelled in order to counterbalance unrealistic energy growth.

When rotation acts alone, there is no production of turbulent energy. An initially isotropic turbulence is acted upon by a solid-body rotation through nonlinear mechanisms only. This is the main specific feature of the problem: in a pure

homogeneous case, any structuring of the flow by rotation is definitely a consequence of nonlinear mechanisms.

Previous experimental studies of homogeneous turbulence primarily concerned cases of pure strain (Batchelor & Proudman 1954; Gence & Mathieu 1979) and shear (Rose 1966; Tavoularis & Corrsin 1981; Bertoglio 1980).

Experimental and theoretical studies devoted to the effects of rotation are more scarce.

The theoretical groundwork on the subject has been recently reinforced. Examining for instance how rotation influences kinetic energy, as proposed by Rogallo (1981), Cambon (1982), the slowing down of its decay can be inferred from phenomenological considerations about overall inertial wave interactions. Concerning the anisotropy of the lengthscales observed by Wigeland & Nagib (1978), contrary to global energy behaviour, such a result cannot be interpreted without an anisotropic phenomenology of nonlinear interactions.

Decisive progress on the subject has been recently made by Cambon & Jacquin (1989), with the aid of a modellization of triple-correlation based on the Eddy Damped Quasi Normal (EDQNM) theory allowing anisotropic effects to be taken into account. Some basic mechanisms were proposed which link the behaviour of both the turbulent energy and the lengthscales to three-dimensional spectral mechanisms. A scenario of transition from a full three-dimensional turbulence towards a two-dimensional one, was proposed.

The full numerical computation of the Navier–Stokes equations in periodic boxes with sufficient resolution is an excellent research tool for this problem. Up to now, the useful numerical results are those of Aupoix *et al.* (1983), Bardina *et al.* (1985), Dang & Roy (1985), Teissèdre & Dang (1987). These numerical experiments have confirmed the decrease in energy in the presence of rotation as well as the anisotropic behaviour of the lengthscales. The latter studies, by Teissèdre & Dang, have focused on the spectral mechanisms described by Cambon & Jacquin (1989). In fact, most theoretical studies are devoted to one-point modelling ($k$-$\epsilon$ and Reynolds stress models) of rotating and curved shear flows. There is a comprehensive review of various contributions in Lakshminarayana (1986); see also the recent contributions of Speziale and colleagues, e.g. Speziale, Gatsti & Mhuiris (1989).

Among the relevant experiments, we may mention those of Traugott (1958), Ibbetson & Tritton (1975), Wigeland & Nagib (1978), Hopfinger, Browand & Gagne (1982), for very different flows.

In Traugott, a rotating turbulence was obtained by means of an air flow passing through several grids in the annular section between two rotating concentric cylinders. The flow was very much influenced by boundary and grid effects, and the solid-body rotation was not achieved.

In the experiment by Hopfinger *et al.*, turbulence was generated by a continuous oscillation of a grid at the bottom of a deep tank of water. They observed singular wave effects together with the presence of quasi-two-dimensional elongated structures in the upper part of the tank. The origin of these large-scale vortices, which have also been found in other experiments in tanks, is still open to question. It seems likely that the influence of rotation on the turbulence generation (here by a transport mechanism), as well as boundary conditions, have to be taken into account in the interpretation of this two-dimensional behaviour (Mory & Caperan 1987).

Ibbetson & Tritton made their measurements in a shallow tank of air and the

turbulence was generated by the sudden displacement of two grids. Their results reflect peculiar dissipative effects induced by interactions between the inertial waves and the boundaries of their apparatus. The dissipation in the Ekman boundaries led to an increase of energy decay in the presence of rotation.

Thus, for one reason or another, all the above experiments are outside the limits of homogeneous turbulence and accordingly out of our scope. The only experimental flow that can be considered as homogeneous is that of Wigeland & Nagib (1978, hereinafter referred to as WN). It concerns the first stage of decay of a rotating grid-generated turbulence. The flow is generated by means of a rotating duct equipped with a honeycomb followed by a grid. In this apparatus, uniform velocity and fluctuation level profiles are obtained and the Ekman dissipation is negligible.

WN performed many experiments corresponding to various combinations of the mean velocity $U$, the rotation rate $\Omega$ and the grid mesh size $M$. The lack of precise theoretical guidelines made this considerable amount of experimental work very difficult to interpret. It is felt that the lack of conclusive results were also due to the small dimensions of the apparatus: the homogeneous core in the last measurement section was small and the probes sizes was not negligible with respect to flow scales. Moreover, measurements were marked by the residual inhomogeneity coming from the rotating grid owing to the fact that the probes were not aligned with the axis of the duct (this arrangement was used to detect curvature effects, which have no meaning in this homogeneous problem).

It was expected that the larger size of the present set-up together with the location of the probes on the duct axis would avoid the main difficulties found in the WN experiment.

Section 2 describes the experimental set-up, and the various measurements performed to qualify the flow. In the beginning of §2, an argument is presented to explain the particular choice of the (three) mesh sizes, the (five) rotation rates and the (one) mean axial velocity.

Section 3 presents the results of the (one-point) measurements. The results concern the principal Reynolds stresses, one-dimensional spectra and associated integral timescales and lengthscales. It is shown that rotation mainly affects the transversal part of the fluctuating field. The search of correlating parameters leads to the definition of Rossby numbers built on the transversal and axial part of the fluctuations, separately. The introduction of these parameters leads to the characterization of a transition between an initial quasi-isotropic regime and a rotation-dominated regime associated to a transversal structuration of the flow.

Our results are compared to those of Wigeland & Nagib in §4.

The four last sections are devoted to various theoretical interpretations of the experimental results.

In §5, we use a simple displaced particle argument (using the terminology of Tritton & Davies 1981 and Tritton 1989) to explain the action of the Coriolis force on the trajectories of the flow particles and its possible consequences on the statistics of the flow.

The theoretical interpretations developed in §§6 and 7 are based on the spectral analysis. The possible impact of the inertial wave regime is first investigated in §6. A distinction is made between the case of a pure homogeneous flow and that of a flow enclosed in a vessel. In the first case, it is shown that the linear regime can lead to strong modifications of the statistics of the flow if the latter is initially non-isotropic. These effects are shown to be weak in our experiment. In the second case, we check

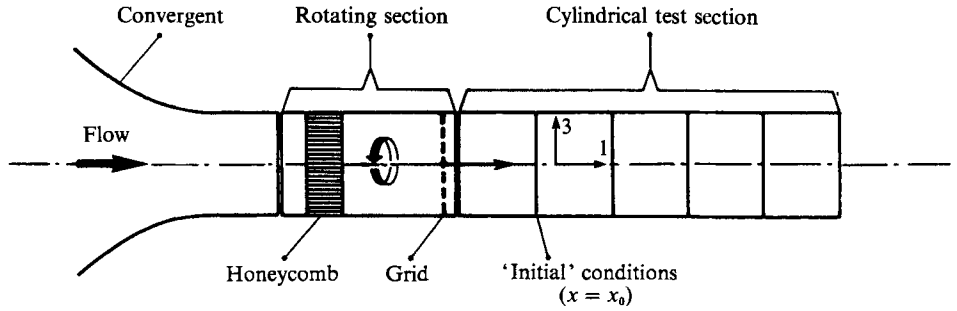


FIGURE 1. Schematic of the experimental set-up (ONERA).

the possible impact of the interaction of the inertial waves with solid boundaries as in the experiment of Ibbetson & Tritton (1975). The anisotropic properties of the flow during the rotation dominated regime are mainly a consequence of nonlinear effects. The spectral phenomenology of a transition towards a two-dimensional turbulence, proposed by Cambon & Jacquin (1989), is confirmed by the experiment.

The body of this study was originally developed in the thesis dissertation of Jacquin (1987). Part of this work was also presented at the 6th Symposium on Turbulent Shear Flows and at the 2nd European Turbulence Conference (Jacquin, Leuchter & Geffroy 1988, 1989). A more extended presentation of the experimental part is given in Jacquin, Leuchter & Geffroy (1990).

## 2. Experimental set-up

The experimental set-up is sketched in figure 1. Solid-body rotation is achieved as in the WN experiment, by a rotating duct equipped with a fine mesh honeycomb. The mesh size and the width of the honeycomb are 1.5 mm and 10 cm, respectively. A rod grid is placed in the downstream part of the rotating duct. The diameter of the duct is 0.3 m. The maximum rotation rate is about 85 rad/s. The second part of the duct is fixed and its length is variable in order to facilitate the exploration of the flow. The maximum length is 1.1 m.

The flow is probed by means of a high precision mechanism allowing displacements in three perpendicular directions. The flow generator, the test section and the probing mechanism are located inside a test chamber from which the flow is extracted by means of a blower located downstream of the test chamber. The maximum axial velocity, $U$, is 20 m/s.

An experimental configuration is defined by a triplet of parameters $(U, \Omega, M)$, with $M$ being the mesh size of the grid which is located inside of the rotating duct. The main limitation of the system is due to the possible blockage induced by strong deflections of the streamlines in the peripherical cells of the honeycomb. For a fixed value of $U$, this happens when $\Omega$ becomes larger than a particular value. This is illustrated on figure 2 which shows the variation of $e'$, the r.m.s. of the voltage delivered by a single hot-wire probe located on the axis of the duct, for three different values of $U$ when $\Omega$ varies. A dramatic increase of $e'$ occurs when $\Omega/U \geqslant 6\ \mathrm{m}^{-1}$, that is when the peripherical angle $\theta$ exceeds arctan $(\Omega r_0/U) \approx 43°$ (with $r_0 = 0.15$ m). This limit corresponds to the occurrence of strong instabilities in the signal. It fixes the maximum rotation rate which can be performed for a particular velocity.

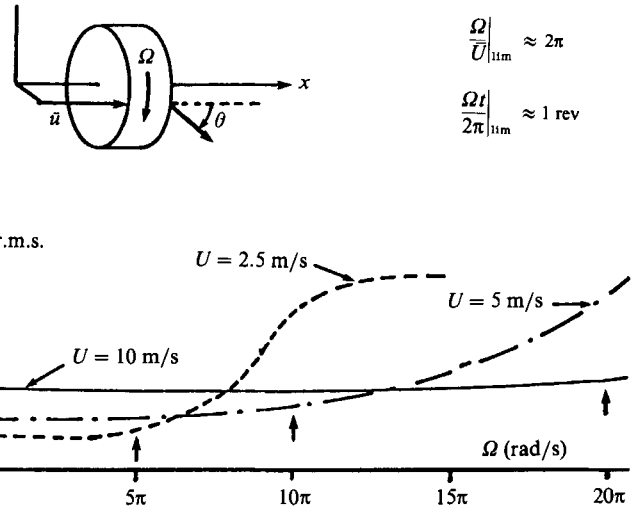


FIGURE 2. Limitation of the rotating generator: variation of the r.m.s. value of a hot wire placed on the axis of the duct for various values of $\Omega$ (rad/s) and $U$ (m/s).

### 2.1. *Determination of an experimental configuration*

The experimental configuration was defined by the following considerations.

It is well known that a grid-generated flow presents some universal properties. In particular, the decay of its energy is well described by means of a power function of $(x/M)$:

$$\frac{q^2(t)}{U^2} = A\left(\frac{x}{M} - \frac{x^*}{M}\right)^{-\alpha}. \tag{2.1}$$

A value of $\alpha = 1.3$ can be inferred from the large number of results available in the literature (see e.g. Comte-Bellot & Corrsin 1966). The origin $x^*/M$ can be physically interpreted as the length necessary for the grid wakes to mix together. From a simple derivation of this relation with respect to $t = x/U$, one can deduce a law for the dissipation rate

$$\epsilon(t) = -\frac{\mathrm{d}(\frac{1}{2}q^2)}{\mathrm{d}t} = \tfrac{1}{2}A\alpha\frac{U^3}{M}\left(\frac{x}{M} - \frac{x^*}{M}\right)^{-(\alpha+1)}, \tag{2.2}$$

and then obtain an expression for the time $\tau$,

$$\tau = \frac{\frac{1}{2}q^2}{\epsilon} = \frac{1}{\alpha}\frac{M}{U}\left(\frac{x}{M} - \frac{x^*}{M}\right)$$

$$= \frac{1}{\alpha}(t - t^*), \tag{2.3}$$

which characterizes the decay of the turbulence. The last relation shows that, for a given location with respect to the grid, $\tau$ depends only on $U$.

The rotation effects can be characterized by a Rossby number equal to the ratio between the rotation time $\tau_\Omega = (2\Omega)^{-1}$ and $\tau$. A first evaluation of this parameter is obtained by supposing $\tau$ to be insensitive to the rotation. This is equivalent to considering that the rotation does not modify the decay law (2.1). This is, of course,

| $U$ (m/s) = 10 | | | | | |
|---|---|---|---|---|---|
| | $\Omega$ (r.p.m.) | 50 | 150 | 300 | 600 |
| | $\Omega$ (rad/s) | 5.24 | 15.7 | 31.4 | 62.8 |
| $M$ = 10 mm | $Ro_M$ | 95.4 | 31.8 | 15.9 | 7.9 |
| | $x/M$ | | 25–113 | | |
| $M$ = 15 mm | $Ro_M$ | 63.6 | 21.2 | 10.7 | 5.3 |
| | $x/M$ | | 16.7–75.3 | | |
| $M$ = 20 mm | $Ro_M$ | 47.7 | 15.9 | 8.0 | 4.0 |
| | $x/M$ | | 12.5–56.5 | | |
| $Ro_q$ (relation (2.4)) | | 12–2 | 4–0.8 | 2–0.4 | 1–0.2 |

TABLE 1. Experimental conditions

certainly false. However, from the WN experiment, the effects of $\Omega$ on $\tau$ are far from being spectacular. From (2.3), one obtains:

$$Ro_q = \frac{\tau_\Omega}{\tau} = \alpha \frac{U}{2\Omega}(x - x^*)^{-1}$$

$$= \alpha \frac{U}{2\Omega M}\left(\frac{x}{M} - \frac{x^*}{M}\right)^{-1}. \tag{2.4}$$

The second relation gives a correspondence between the grid mesh Rossby number $Ro_M = U/2\Omega M$ and the macroscale Rossby number $Ro_q$. The first relation shows that $Ro_q$ depends on $U/\Omega$. As we said above, this ratio cannot be less than about $\frac{1}{6}$ m owing to instabilities induced by the honeycomb below this limit. This value fixes a minimum for $Ro_q$. For $\alpha = 1.3$ and $x^*/M = 3$, this minimum is about 0.2 at the end of the test duct. However, if, as expected, the rotation slows the decay of $q^2$, this would lead to an increase of $\tau$ and to smaller values of $Ro_q$.

The mesh size $M$ will fix the lengthscales of the flow which must be sufficiently large with respect to the probe size. In accordance with (2.1) and (2.3), it will also determine the range of variation of the kinetic energy $\frac{1}{2}q^2$ or equivalently that of the decay time $\tau$.

Three values $M$ = 10, 15 and 20 mm were tested. A mean velocity of $U$ = 10 m/s was chosen to make use of about the whole capacity of the rotation generator with four rotation rates between 5 and 63 rad/s.

The experimental configurations are summarized in table 1.

This makes it possible for $Ro_q$ to span about two decades.

### 2.2. *Measurement techniques*

For the turbulence measurements we used DISA P61 crossed hot-wire probes and DISA 55M01 anemometers with a 55M10 standard bridge. A PRESTON GMAD-1 converter and an HP 1000 digital data acquisition system were used to process the signals. The acquisitions correspond to following parameters: digitization frequency 8000 Hz; low-pass filtering 3150 Hz; buffer length 100 blocks of 2048 values (for each wire).

The velocity components were obtained by numerical interpolations of numerical charts generated during the calibrations of the hot-wire probes.

Frequency spectra of the fluctuating velocity components are also provided by means of classical FFT techniques.

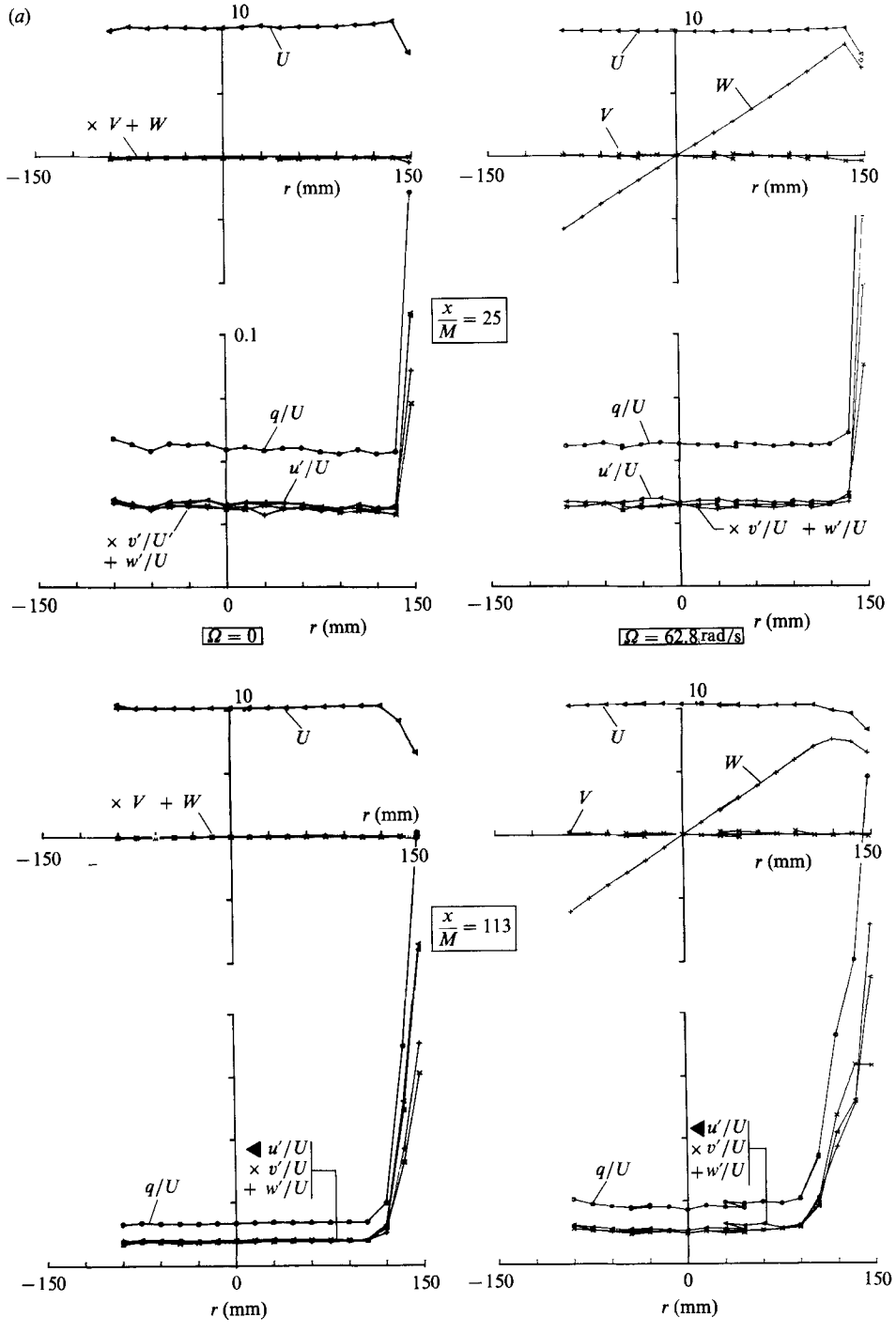


FIGURE 3(*a*). For caption see page 9.

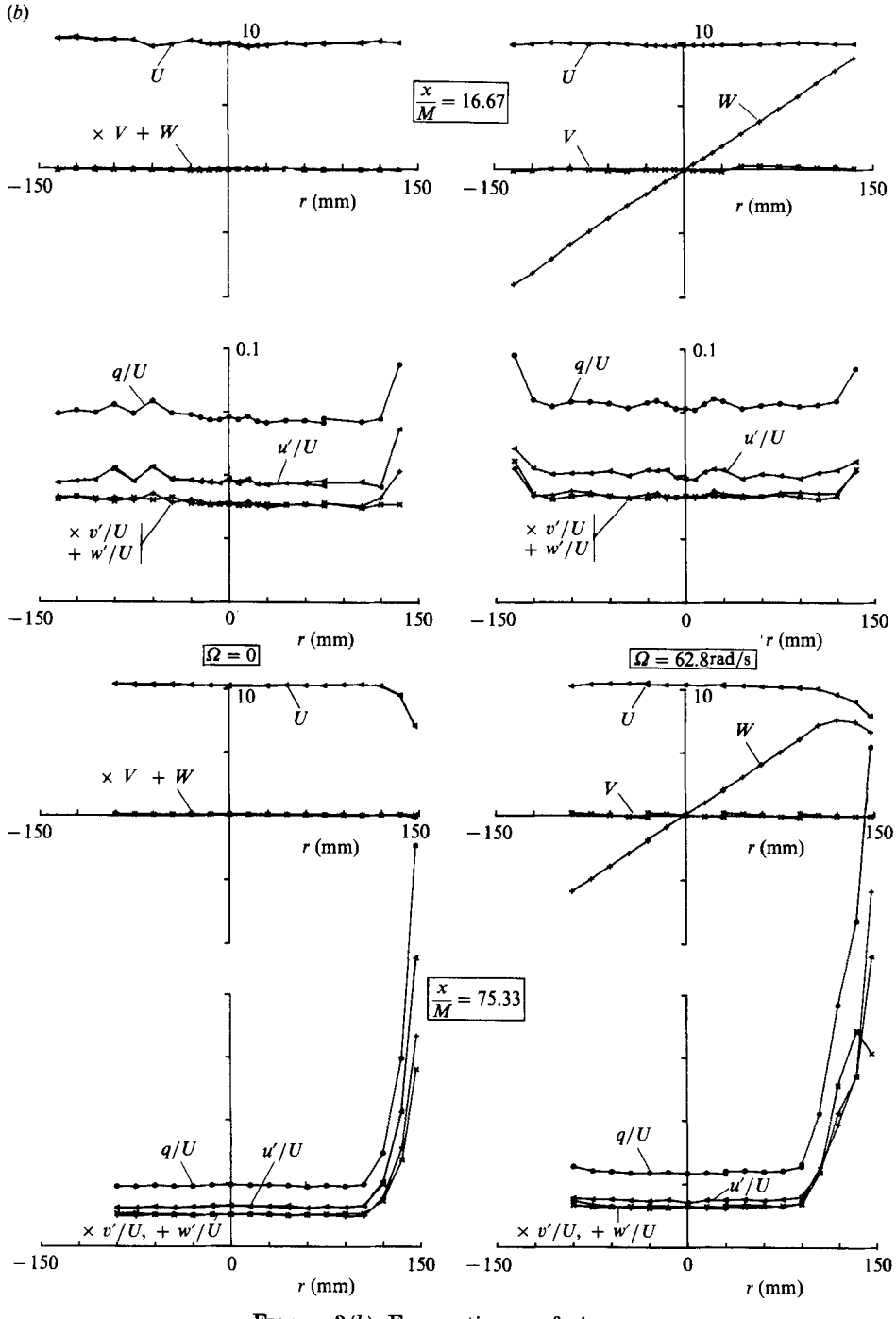


FIGURE 3(b). For caption see facing page.

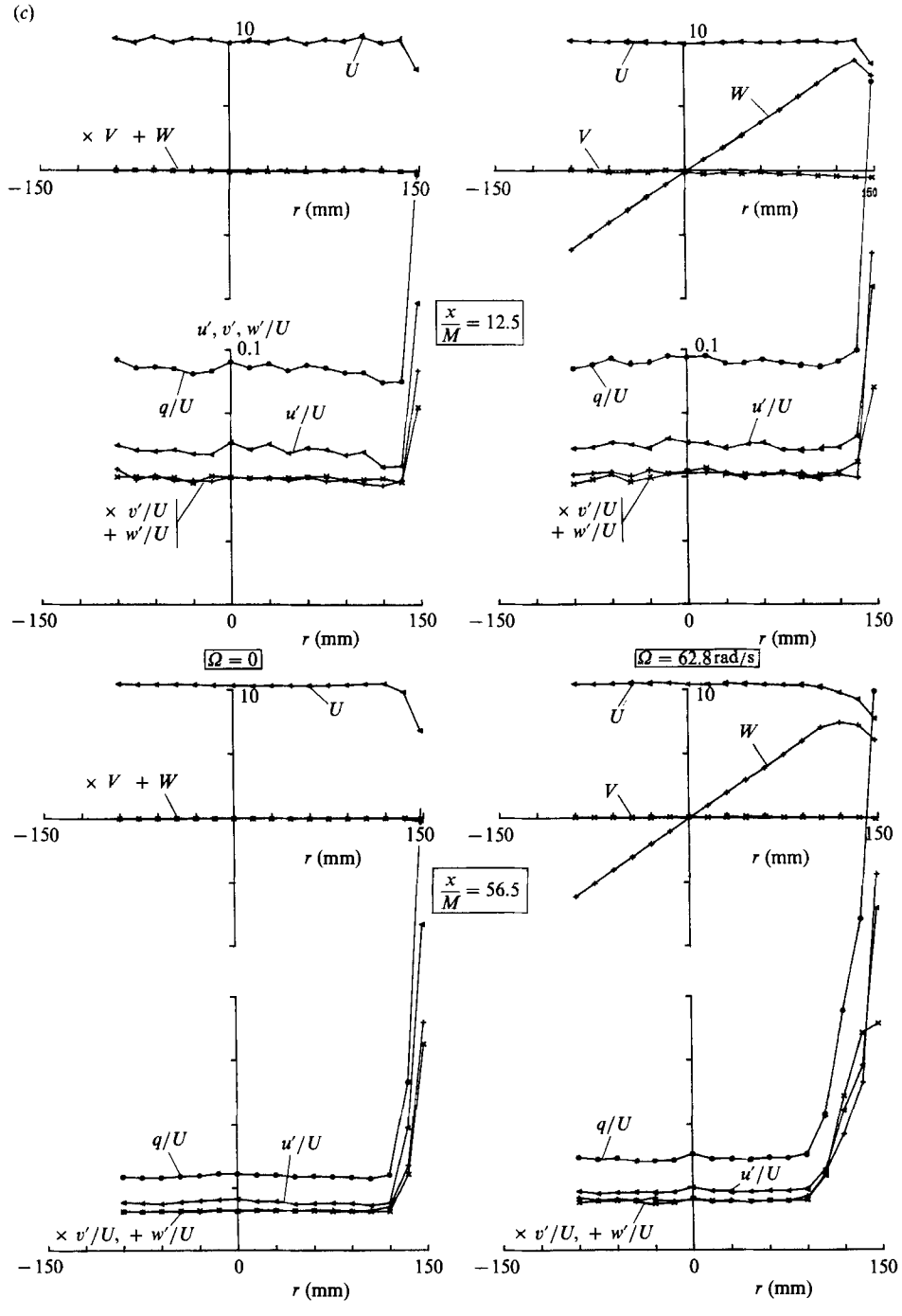


FIGURE 3. Mean profiles in the first and last test sections, for $\Omega = 0$ and 62.8 rad/s: (*a*) $M = 10$ mm, (*b*) $M = 15$ mm, (*c*) $M = 20$ mm.

### 2.3. *Qualification of the flow*

Figure 3 shows the mean velocity and r.m.s. distributions in the first and the last test sections of the duct for $\Omega = 0$ and $\Omega = 62.8$ rad/s. Figures 3(*a*)–3(*c*) correspond to the three different mesh sizes. For these measurements the probes are translated along the horizontal axis $y$, and, for $\Omega \neq 0$, they are reorientated several times to minimize their incidence with respect to the swirling mean streamlines. The traverse mechanism cannot span a whole diameter, which is why the profiles are incomplete. The radial component, $V$, is measured with a horizontal orientation of the plane of the wires, and the tangential component, $W$, with a vertical orientation.

These figures show that in the presence of rotation the tangential profiles are perfectly rectilinear and well preserved along the duct. The mean solid-body rotation, which is a necessary condition for the existence of homogeneous rotating turbulence, is thus well achieved.

Concerning the fluctuations, in the first test section the profiles exhibit some variations which are due to the position very close to the grid and to slight residual rotating inhomogeneities coming from the grid. Further downstream, the inhomogeneities have been smoothed out so that very satisfactory conditions for homogeneity prevail. Note that the boundary layer has developed but the core of solid-body rotation is still about 200 mm in diameter at the end of the duct.

The levels of the respective components $u'$, $v'$ and $w'$ as well as their sensitivity to the rotation will be extensively discussed in the subsequent sections.

## 3. Characterization of rotation effects

All the measurements corresponding to table 1 of §2.1 have been performed on the axis of the duct.

### 3.1. *Kinetic energy*

Figure 4 shows the decay of (twice) the kinetic energy $q^2 = u'^2 + v'^2 + w'^2$ for all cases of table 1. The values corresponding to the various rotation rates and the reference cases $\Omega = 0$ are brought together with suitable translations of the vertical axis. Figure 4(*a*)–4(*c*) correspond to the three different mesh sizes. Figure 4(*d*) shows the power laws which can be inferred from the results of figure 4(*b*) (the respective values of the exponent and of the origin are indicated on the curves).

Considering the cases without rotation, if one introduces a fictitious origin $x^*$ and an exponent $\alpha$ to obtain the best power-law fit (2.1) (in the least-square sense) on these values of $q^2$ one obtains the results shown in table 2. The various values of $x^*/M$ and $\alpha$ lie in the range of previous results of grid-generated turbulence. The second of these laws corresponds to the curve at the bottom of figure 4(*d*).

Figure 4(*a–c*) shows that rotation slows the decay of $q^2$: the larger $\Omega$, the more intense is this effect.

Considering figure 4(*d*), the possibility of smoothing the set of ten experimental points by means of the two parameters $x^*/M$ and $\alpha$ is not surprising from a technical point of view. In the authors' opinion, these results have no particular physical meaning. They are given for the purpose of illustrating the gradual slowing down of the turbulence decay under the effect of rotation.

### 3.2. *One-dimensional spectra*

Figure 5 shows the power spectral density functions $E_u$ and $E_v$ obtained for $\Omega = 0$ and for $\Omega = 62.8$ rad/s in the different sections of the duct. Figures 5(*a*), 5(*b*) and 5(*c*)

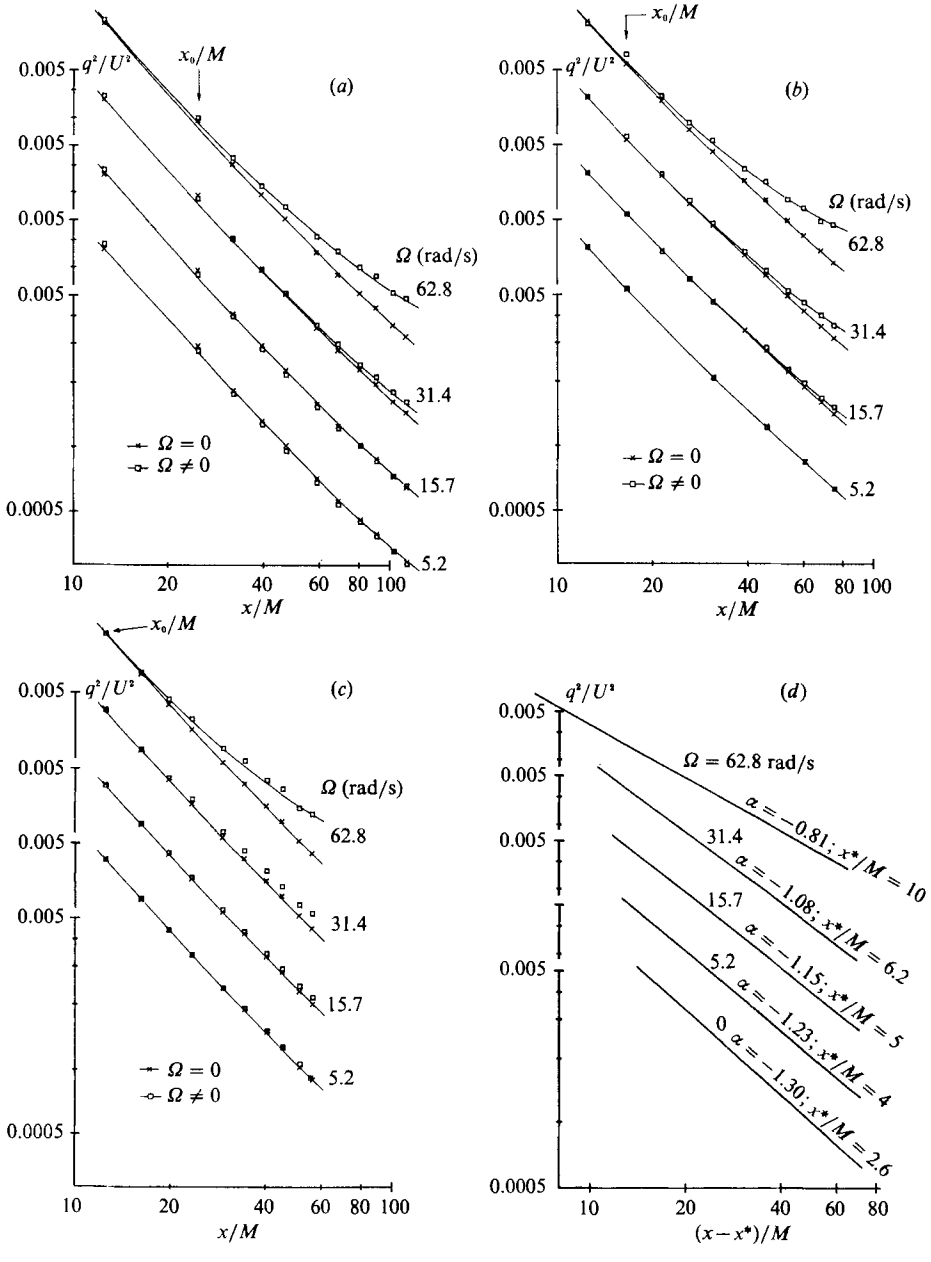


FIGURE 4. Decay of the kinetic energy at various $\Omega$: (*a*) $M = 10$ mm, (*b*) $M = 15$ mm, (*c*) $M = 20$ mm, (*d*) power laws for $M = 15$ mm.

| $M$ | $A$ | $x^*/M$ | $\alpha$ |
|---|---|---|---|
| 10 mm | 0.263 | 1.69 | 1.45 |
| 15 mm | 0.151 | 2.60 | 1.30 |
| 20 mm | 0.275 | 1.82 | 1.43 |

TABLE 2

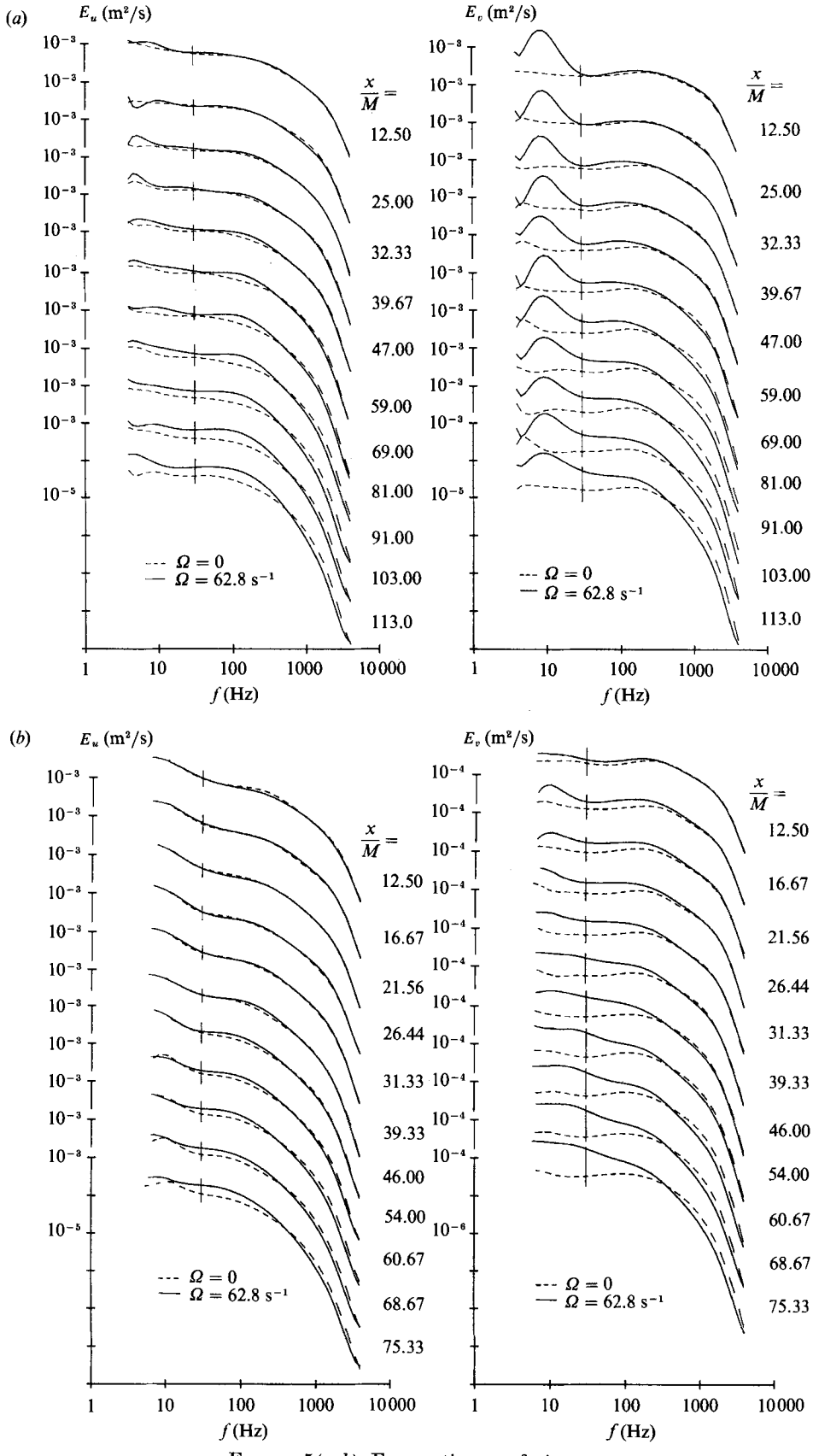


FIGURE 5(*a*, *b*). For caption see facing page.

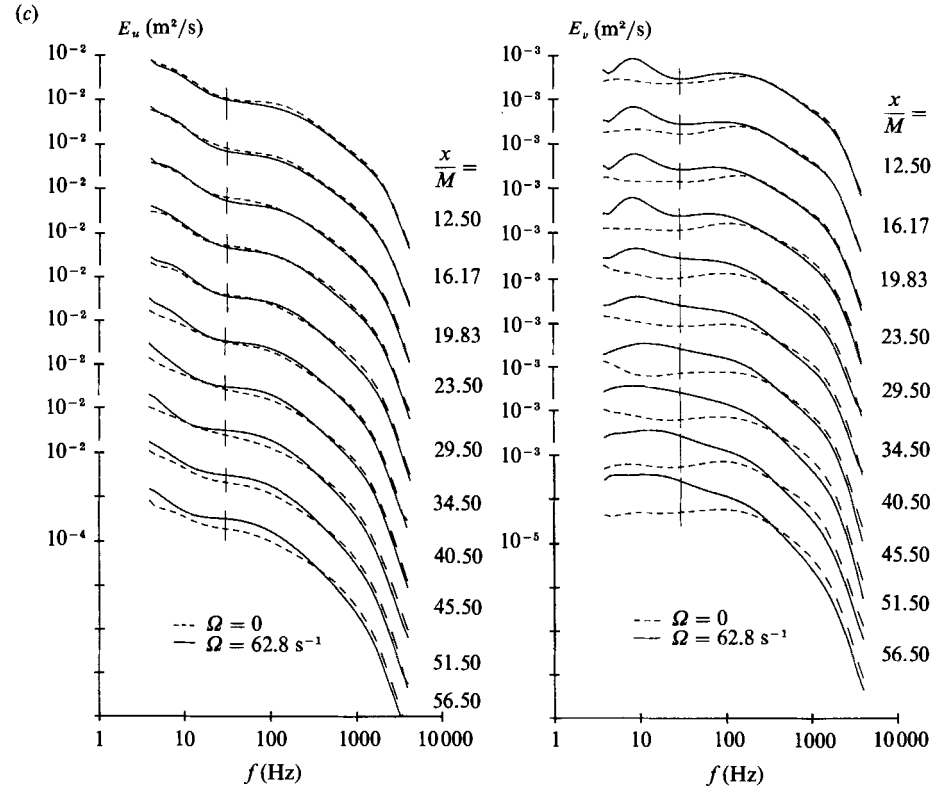


FIGURE 5. Energy spectral density function of $u$ and $v$ signals at $\Omega = 0$ and 62.8 rad/s in different positions: (*a*) $M = 10$ mm, (*b*) $M = 15$ mm, (*c*) $M = 20$ mm.

give the results for each of the three mesh sizes. The curves correspond to smoothing of FFT estimators with order ten Chebyshev polynomials.

Figure 5(*a*), shows that, with rotation an extraneous low-frequency contribution to $E_v$ appears. This bump, located in the range of frequency around $\Omega/2\pi \approx 10$ Hz, results from residual inhomogeneities coming from the rotating grid. As the mesh size increases, the magnitude of the low-frequency components becomes higher than that of the bump and the latter disappears as shown on figure 5(*b*) and 5(*c*). However, it is now $E_u$, which is affected by an extraneous low-frequency energy in the range $f < 30$ Hz. This phenomenon is observed at $\Omega = 0$ and is independent of the rotation.

Some tests have shown that this extraneous contribution was induced by a longitudinal pulsation of the flow caused by the discontinuity of the test duct in the test chamber (see figure 1) and that this mechanism interacted with the largest scales of the flow. This interaction increased with the level of the energy associated with the largest scales, this energy being fixed by the mesh size of the grid in the apparatus: this extraneous energy cannot be detected in the spectra corresponding to the smaller mesh size $M = 10$ mm (figure 5*a*) whereas its contribution to $u'^2$ can go as high as 22% for the 20 mm grid (figure 5*c*).

The increase in the ratio $u'^2/v'^2$ with $M$ at $\Omega = 0$, which is inferred from figure 3, is essentially due to this phenomenon.

For $U = 10$ m/s, the value $f_D = 30$ Hz corresponds to flow structures which have the same length as the diameter $D$ of the duct. This correspondence has been confirmed by changing $U$. The range $f < f_D$ thus corresponds to structures which are outside the limit of homogeneity.

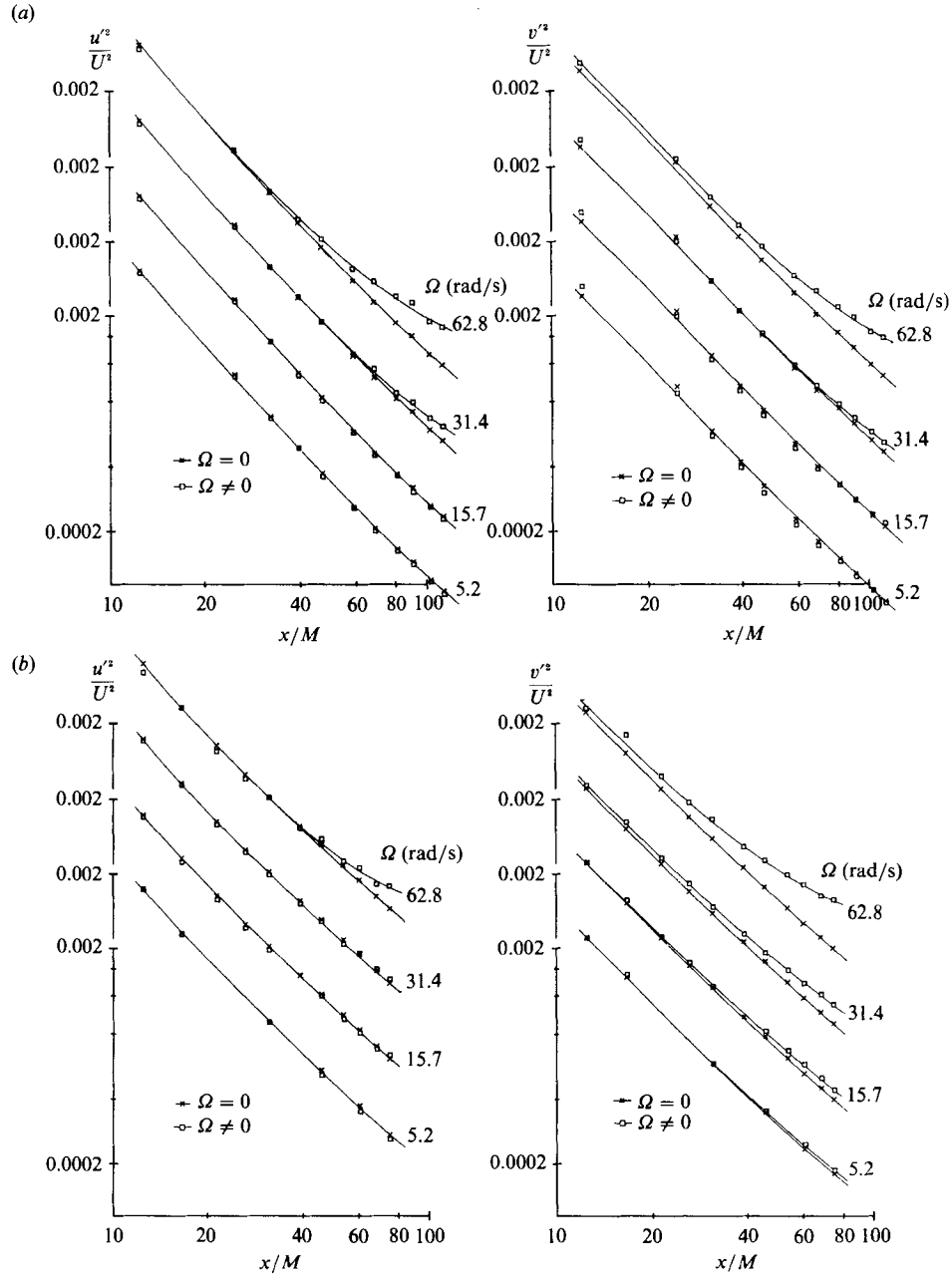


FIGURE 6(*a*, *b*). For caption see facing page.

One possibility was to filter out the signals below $f_D$. Another was to fix the value of $E_u(f)$ at $E_u(f_D)$ for $f < f_D$. These procedures were tested during preliminary investigations of the flow. Their consequences on different aspects of the results presented herein have been found to be negligible. In view of the arbitrariness of these treatments we have decided to keep things unchanged. As will be explained later, only the integral lengthscales required suitable corrections on account of this problem.

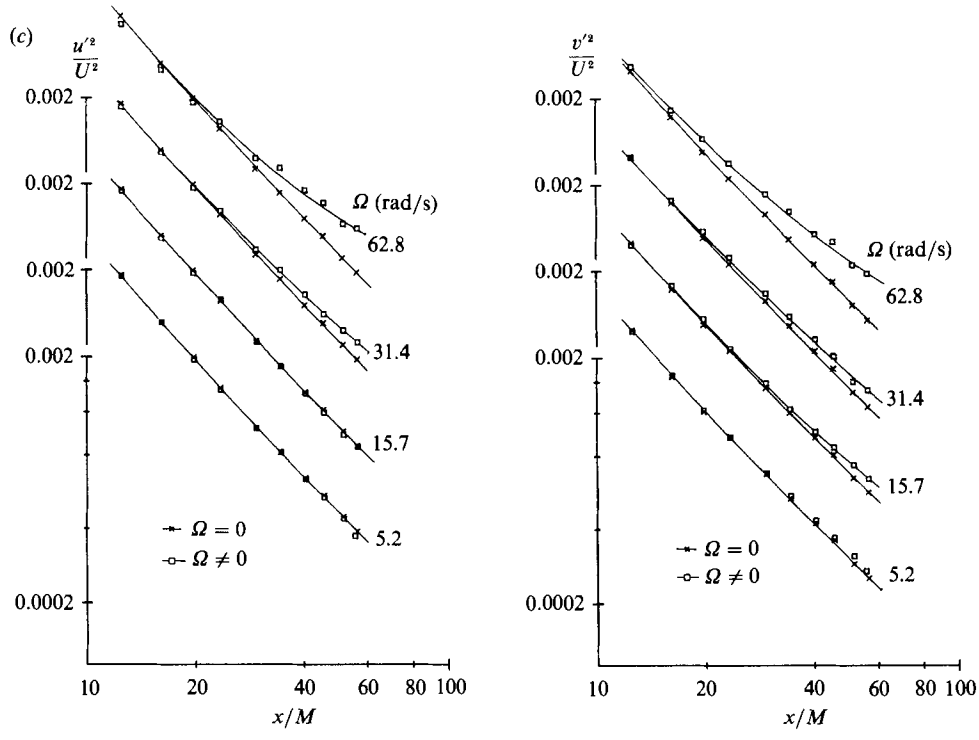


FIGURE 6. Decay of the individual normal stresses $u'^2$ and $v'^2$ for various $\Omega$: (*a*) $M = 10$ mm, (*b*) $M = 15$ mm, (*c*) $M = 20$ mm.

Concerning the effects of rotation on $E_u$ and $E_v$ aside from the range $f < f_D$, strong modifications are observed. In the mid-frequency range, the slopes are accentuated as a consequence of a lessening of the energy in the high-frequency range and an increase in the low-frequency range. The spectra for the transverse fluctuation component $E_v$ is much more affected by a spectacular increase of the low-frequency contribution.

If we ignore this anisotropic aspect, these curves substantiate the following global phenomenology: rotation inhibits the transfer of energy from large scales to smaller scales; this results in a lessening of the dissipative process and, consequently, in a slowing of the kinetic energy decay.

The differences observed between the $E_u$ and $E_v$ spectra is evidence that the above process is strongly non-isotropic and that it mainly affects the transverse part of the fluctuating field. This point will be thoroughly examined in the subsequent sections.

### 3.3. *Normal stresses*

Figure 6 shows the evolutions of $u'^2$ and $v'^2$ ($\approx w'^2$) and figure 7, that of the structural parameter

$$K = \frac{u'^2 - v'^2}{u'^2 + v'^2} \tag{3.1}$$

introduced by Townsend (1954) to characterize the anisotropy of the Reynolds stress tensor. This anisotropy could also be characterized by the invariants of this tensor. Parts (*a*), (*b*) and (*c*) of figures 6 and 7 show the results corresponding to each of the three mesh sizes. Several remarks may be made about these figures.

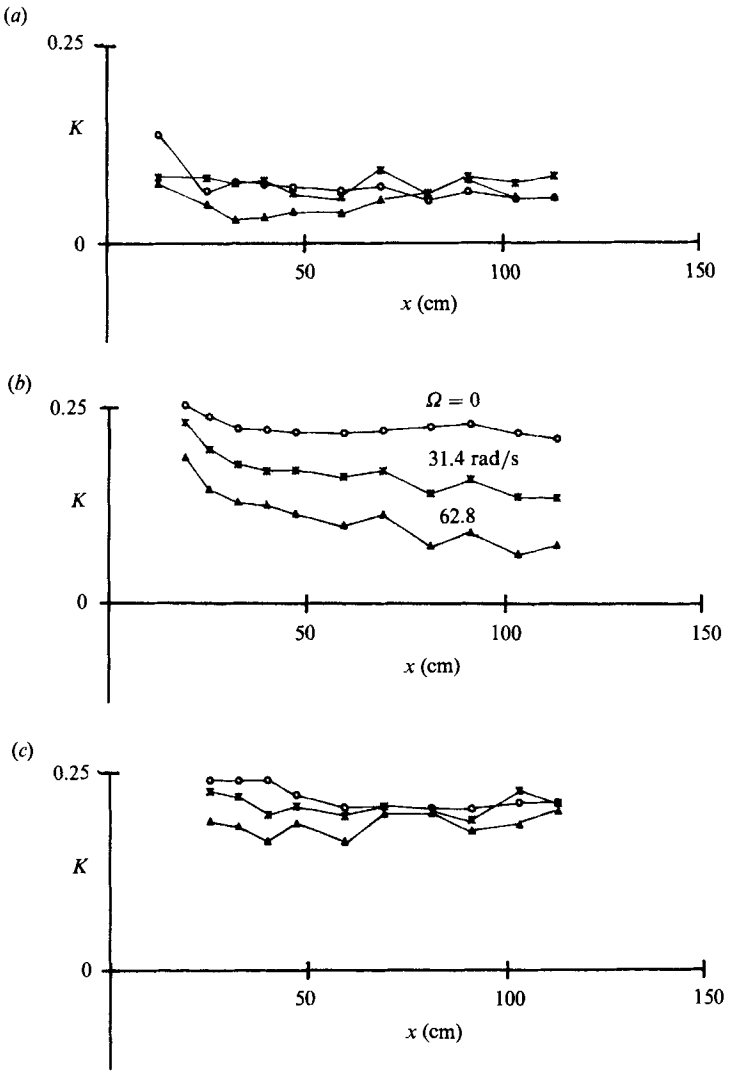


FIGURE 7. Structural parameter $K = (u'^2 - v'^2)/(u'^2 + v'^2)$: (a) $M = 10$ mm, (b) $M = 15$ mm, (c) $M = 20$ mm.

Figure 6 shows that rotation slows the decay of both components, but different behaviours are observed depending on the mesh size: for $M = 10$ mm (a), and $M = 20$ mm (c), $u'^2$ and $v'^2$ are equally affected, whereas for $M = 15$ mm (b), $u'^2$ is affected little with respect to $v'^2$. This is confirmed by figure 7 where a quasi-invariance of $K$ is observed for $M = 10$ and 20 mm, whereas for $M = 15$ mm, a damping of the anisotropy is obtained according to the decrease of $K$ with $x/M$ and $\Omega$. This difference has not yet been explained.

Thus, except perhaps for $M = 15$ mm, the normal stresses do not reflect the anisotropic mechanisms of rotation which are expected from the changes in the one-dimensional spectra of figure 5.

The increase of $K$ for $\Omega = 0$ between the case $M = 10$ mm and $M = 15$ mm or $M = 20$ mm is directly associated with the emergence of extraneous energy in the range $f < 30$ Hz of $E_u$ (see previous section).

### 3.4. *Integral lengthscales*

The integral lengthscale $L_{ij,l}$ is the mean correlation length between the components $u_i$ and $u_j$ of the fluctuations measured at different locations with separations along the $l$-axis:

$$L_{ij,l} = \int_0^\infty \frac{\langle u_i(\boldsymbol{x})\, u_j(\boldsymbol{x}+r\boldsymbol{i}_l)\rangle}{\langle u_i(\boldsymbol{x})\, u_j(\boldsymbol{x})\rangle}\,\mathrm{d}r. \tag{3.2}$$

The integral lengthscales that have been investigated in the present experiment are $L_{11,1}$ and $L_{22,1}(\approx L_{33,1})$: these scales are mean correlations between $u$ or $v$ fluctuations considering axial separations (along the rotation axis). For convenience they will be denoted $L_u$ and $L_v(\approx L_w)$, respectively.

In practice, these quantities may be found from the time correlations of $u$ and $v$ signals. For this, relation (3.2) is transformed in the framework of ergodicity and using the Taylor 'frozen field' hypothesis.

Equivalently, they can be calculated (with the same assumptions) from the power spectral density functions $E_u(f)$ and $E_v(f)$. The relations are written:

$$\left.\begin{aligned} L_u &= \frac{U}{4u'^2} E_u(f=0), \\ L_v &= \frac{U}{4v'^2} E_v(f=0). \end{aligned}\right\} \tag{3.3}$$

As the zero frequency corresponds to records of infinite length it is not accessible in the experiment. An extrapolation down to the origin of the available spectral estimators is then necessary (see Comte-Bellot & Corrsin (1966) for a discussion on this point). This procedure becomes very questionable in the presence of the extraneous low-frequency contributions to $E_u(f)$ in figure 5. This bump in the spectra corresponds to long oscillations of the tails of the time correlation and an equivalent difficulty would be encountered in evaluating the integrals of such functions.

In order to overcome this difficulty, we have replaced $f = 0$ in relations (3.3) by $f = f_D = 30$ Hz:

$$\left.\begin{aligned} L_u &= \frac{U}{4u'^2} E_u(f=f_D), \\ L_v &= \frac{U}{4v'^2} E_v(f=f_D). \end{aligned}\right\} \tag{3.4}$$

As we said in §3.2, the limit $f_D$ of the low-frequency bump, corresponds to the diameter of the duct. Looking at $E_v$ in figure 5, this change of definition does not affect $L_v$ for $M = 15$ mm and 20 mm because of the very flat initial shape of $E_v$; for $M = 10$ mm, $f_D$ lies outside the frequency range of residual grid inhomogeneity effects (around 10 Hz). This change of definition does not significantly affect $L_u$ in the case of the smaller grid, the spectra $E_u$ being regular in this case.

An alternative would consist of both filtering the $u$-signal with a high-pass cutoff frequency of 30 Hz and substituting the energy of this signal for $u'^2$ in (3.4). Preliminary investigations have led us to the conclusion that, whatever the rotation rate is, this new definition changes the level of $L_u$ but not its evolution law. In consequence, (3.4) have been adopted for the definition of $L_u$ and $L_v$.

Figure 8 shows the variation of $L_u$ and $L_v$ versus $x/M$ at $\Omega = 0$. In a grid-generated

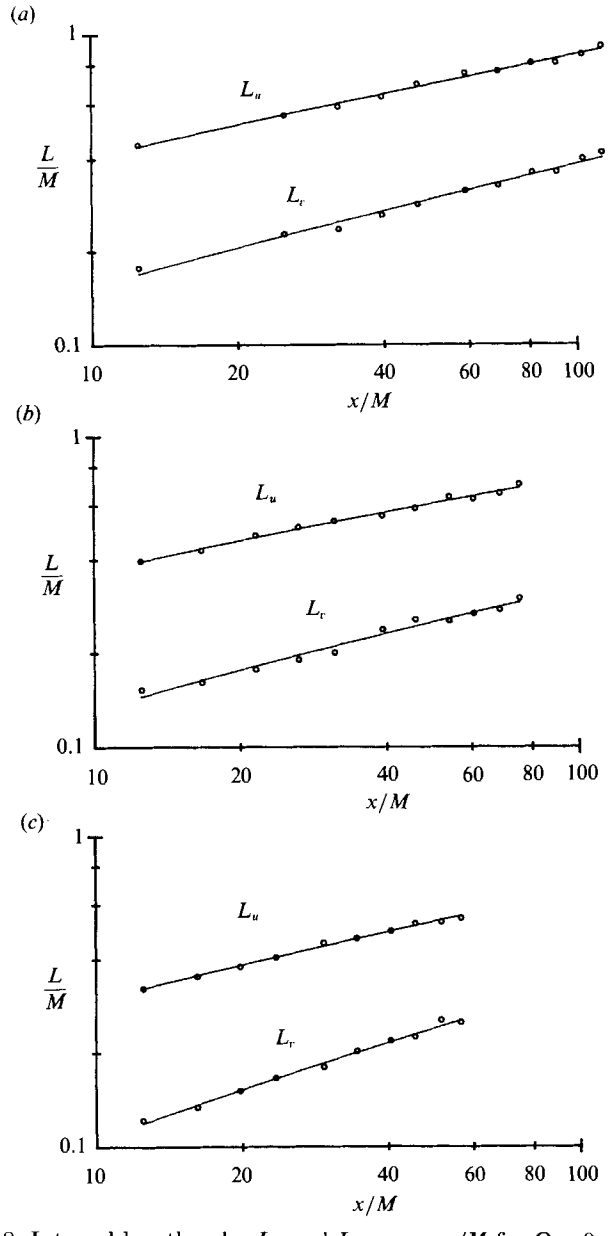


FIGURE 8. Integral lengthscales $L_u$ and $L_v$ versus $x/M$ for $\Omega = 0$: (a) $M = 10$ mm, (b) $M = 15$ mm, (c) $M = 20$ mm.

| $M$ | $x^*/M$ | $B_u$ | $\beta_u$ | $B_v$ | $\beta_v$ |
|---|---|---|---|---|---|
| 10 mm | 1.69 | 0.212 | 0.303 | 0.070 | 0.375 |
| 15 mm | 2.78 | 0.211 | 0.273 | 0.066 | 0.345 |
| 20 mm | 1.82 | 0.147 | 0.330 | 0.040 | 0.462 |

TABLE 3

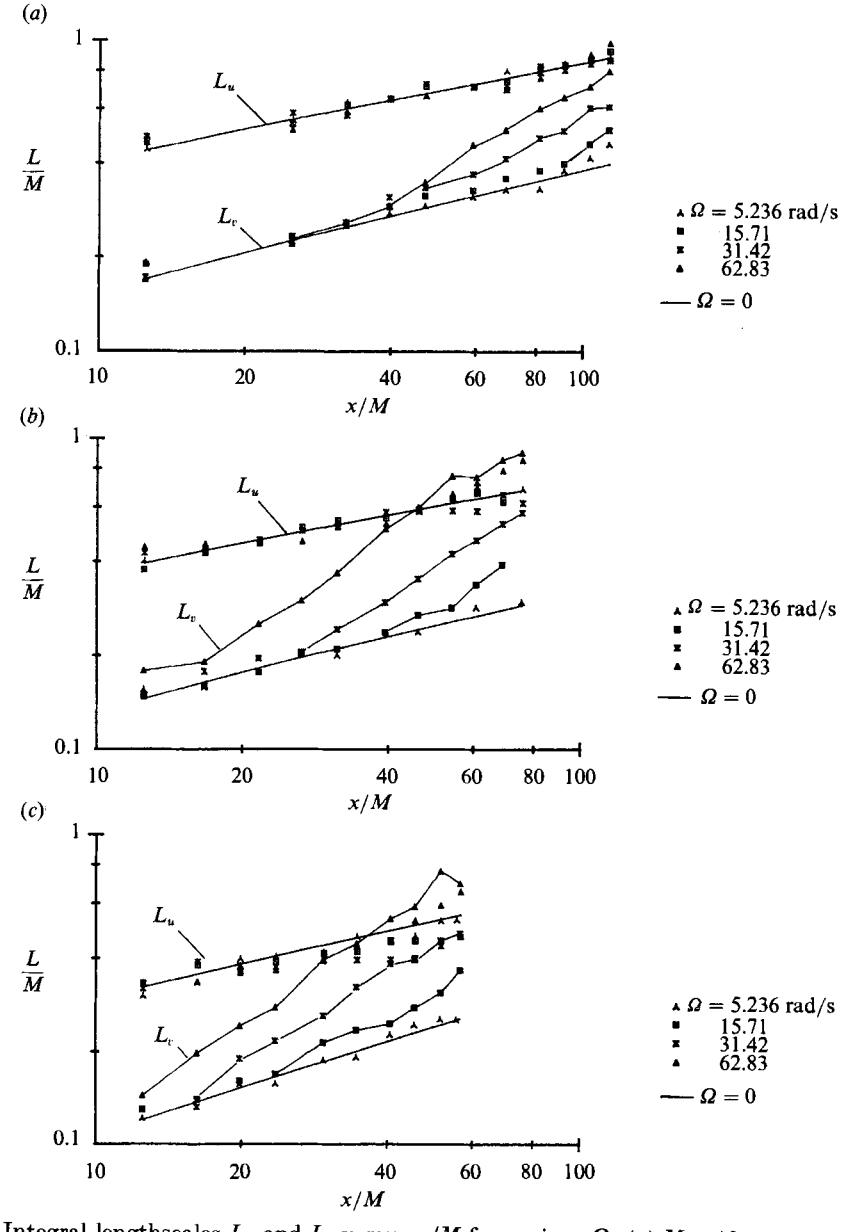


FIGURE 9. Integral lengthscales $L_u$ and $L_v$ versus $x/M$ for various $\Omega$: (*a*) $M = 10$ mm, (*b*) $M = 15$ mm, (*c*) $M = 20$ mm.

turbulence, as concerns the kinetic energy, these scales are usually described by power laws of the type:

$$\left.\begin{aligned} \frac{L_u}{M} &= B_u\left(\frac{x}{M}-\frac{x^*}{M}\right)^{\beta_u}, \\ \frac{L_v}{M} &= B_v\left(\frac{x}{M}-\frac{x^*}{M}\right)^{\beta_v}. \end{aligned}\right\} \tag{3.5}$$

From figure 8, one obtains table 3. Classical results correspond to $\beta_u \sim 0.35$, $\beta_v \sim 0.30$ and $L_u > 2L_v$ (see e.g. Comte-Bellot & Corrsin 1971). Note that $L_u = 2L_v$ in the

case of a strictly isotropic turbulence. The exponent $\beta_u$ found in the present experiment is thus smaller than that found in previous studies. This is most likely to be a consequence of the particular behaviour of the low-frequency part of $E_u(f)$.

Figure 9 shows how $L_u$ and $L_v$ vary in the presence of rotation. The straight lines correspond to the cases without rotation of figure 8. As it could be inferred from the shapes of the spectra in figure 5, rotation has a more pronounced influence on the transverse scale $L_v$ than it has on the axial one, $L_u$: when $\Omega$ increases, $L_v$ departs quite abruptly from its initial behaviour and then increases faster. The higher $\Omega$ is, the closer to the grid this change occurs. This second regime for $L_v$ is well described by a power law with an exponent close to unity, so that $L_v$ becomes approximately proportional to the time $t (\approx x/U)$. $L_u$ is affected little, behaving mostly as if there were no rotation. The only exception is for $M = 15$ mm and 20 mm, for the largest rotation rate and the larger $x/M$. Note that in this case $L_v$ is now larger than $L_u$.

These results show that rotation strongly increases the lateral coherency of the fluctuations. Moreover this effect seems to be triggered for particular values of $x/M$. The existence of this transition-like change of behaviour is of great interest and will be characterized soon.

### 3.5. *Rossby numbers*

On the whole, quite different behaviours are observed for the quantities built on the axial or transversal components of the fluctuations. A separate analysis of the two components can be pursued in the following way. From $u'$, $v'$, $L_u$ and $L_v$ one can examine the timescales built on these quantities. Consider the times:

$$\left.\begin{aligned} \tau_u &= \frac{L_u}{u'}, \\ \tau_v &= \frac{2L_v}{v'}, \end{aligned}\right\} \tag{3.6}$$

which characterize the dynamics of each fluctuation component. With a normalization by the rotation time $\tau_\Omega = (2\Omega)^{-1}$, we get the following Rossby numbers:

$$\left.\begin{aligned} Ro_u &= \frac{\tau_\Omega}{\tau_u} = \frac{u'}{2\Omega L_u}, \\ Ro_v &= \frac{\tau_\Omega}{\tau_v} = \frac{v'}{4\Omega L_v}. \end{aligned}\right\} \tag{3.7}$$

Figure 10 shows the behaviour of these parameters as a function of $x/M$. The two Rossby numbers have different behaviours: on the whole, $Ro_u$ tends to decrease more slowly whereas $Ro_v$ decays faster; the latter effect, which is more pronounced than the first one, seems to be triggered at particular values of $x/M$ which depend on $\Omega$.

According to (3.7), for a given $\Omega$, $Ro_u$ and $Ro_v$ behave respectively as $\tau_u^{-1}$ and $\tau_v^{-1}$. Thus, through the results of figure 10, one of the main effects of rotation appears to be a strong increase in the characteristic time of the transverse fluctuation components. This behaviour is associated with a strong increase of the lateral lengthscale $L_v$, which is not compensated for by a slower decay of the Reynolds stress tensor component $v'^2$; correlatively, as observed in figure 5, the shape of the one-dimensional spectrum $E_v$ is greatly transformed.

Moreover, figure 10 sheds new light on a transition-like separation between two regimes which were observed in the lengthscales variation. In the figure, the change

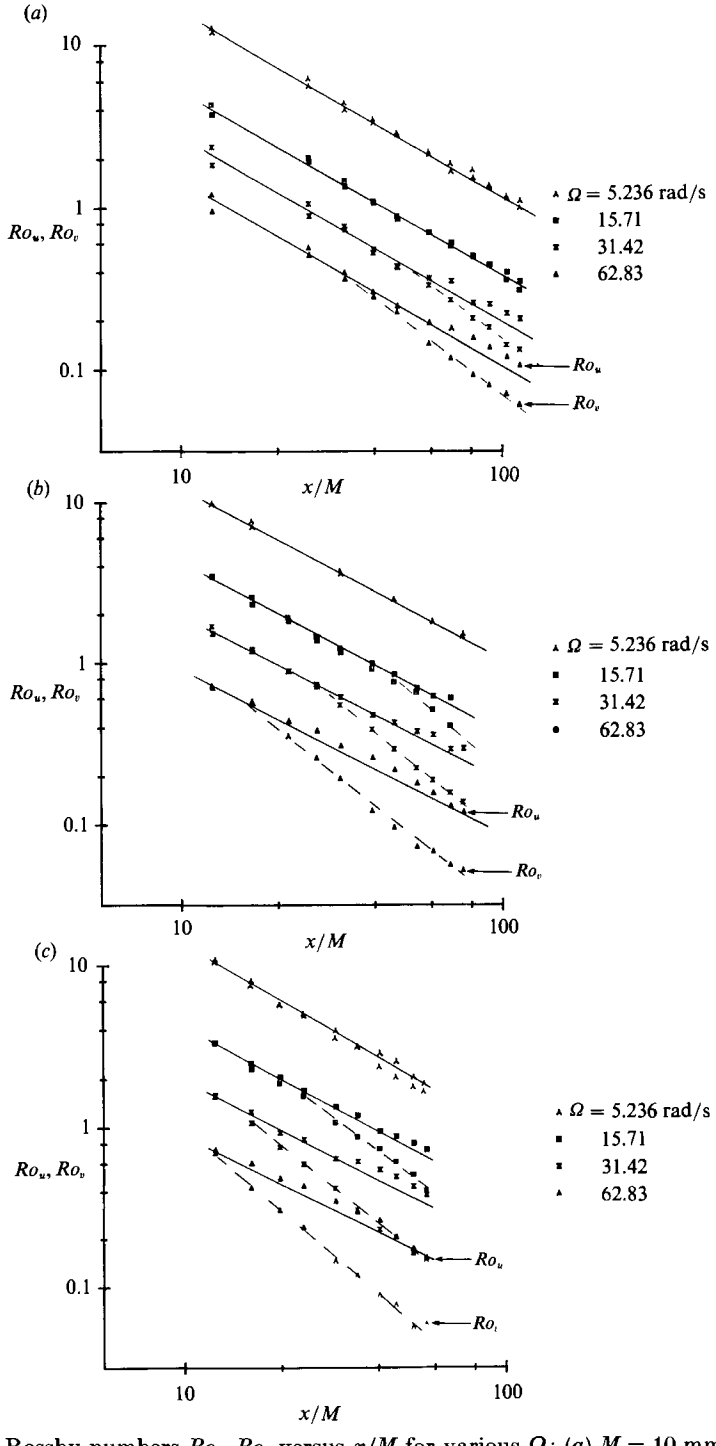


FIGURE 10. Rossby numbers $Ro_u, Ro_v$ versus $x/M$ for various $\Omega$: (*a*) $M = 10$ mm, (*b*) $M = 15$ mm, (*c*) $M = 20$ mm.

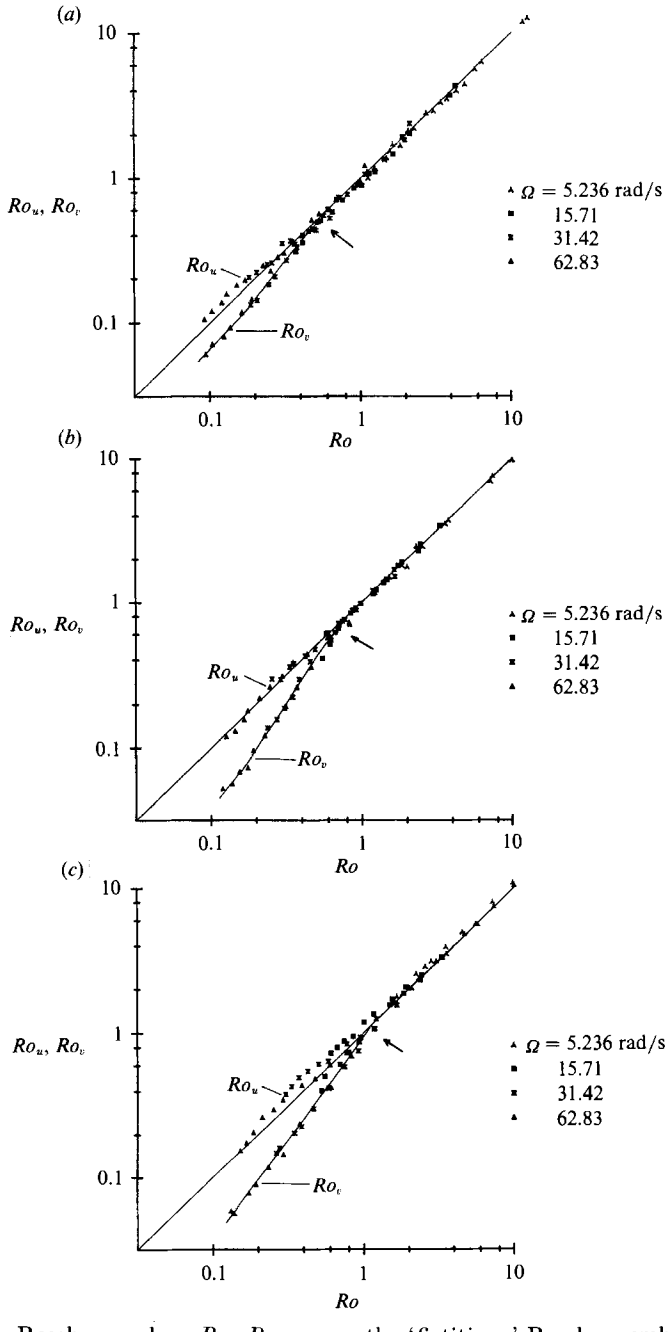


FIGURE 11. Rossby numbers $Ro_u, Ro_v$ versus the 'fictitious' Rossby numbers $Ro^*$: (a) $M = 10$ mm, (b) $M = 15$ mm, (c) $M = 20$ mm.

of behaviour of $Ro_v$ corresponds to a particular value of this parameter, e.g. less than unity. The exact value seems to depend on the mesh size. Thus, the rotation dominated regime corresponds to $Ro_u$ and $Ro_v < 1$. Such a result is in accordance with the definition of these parameters, but the transition observed at a value about equal to unity is surprisingly clear here.

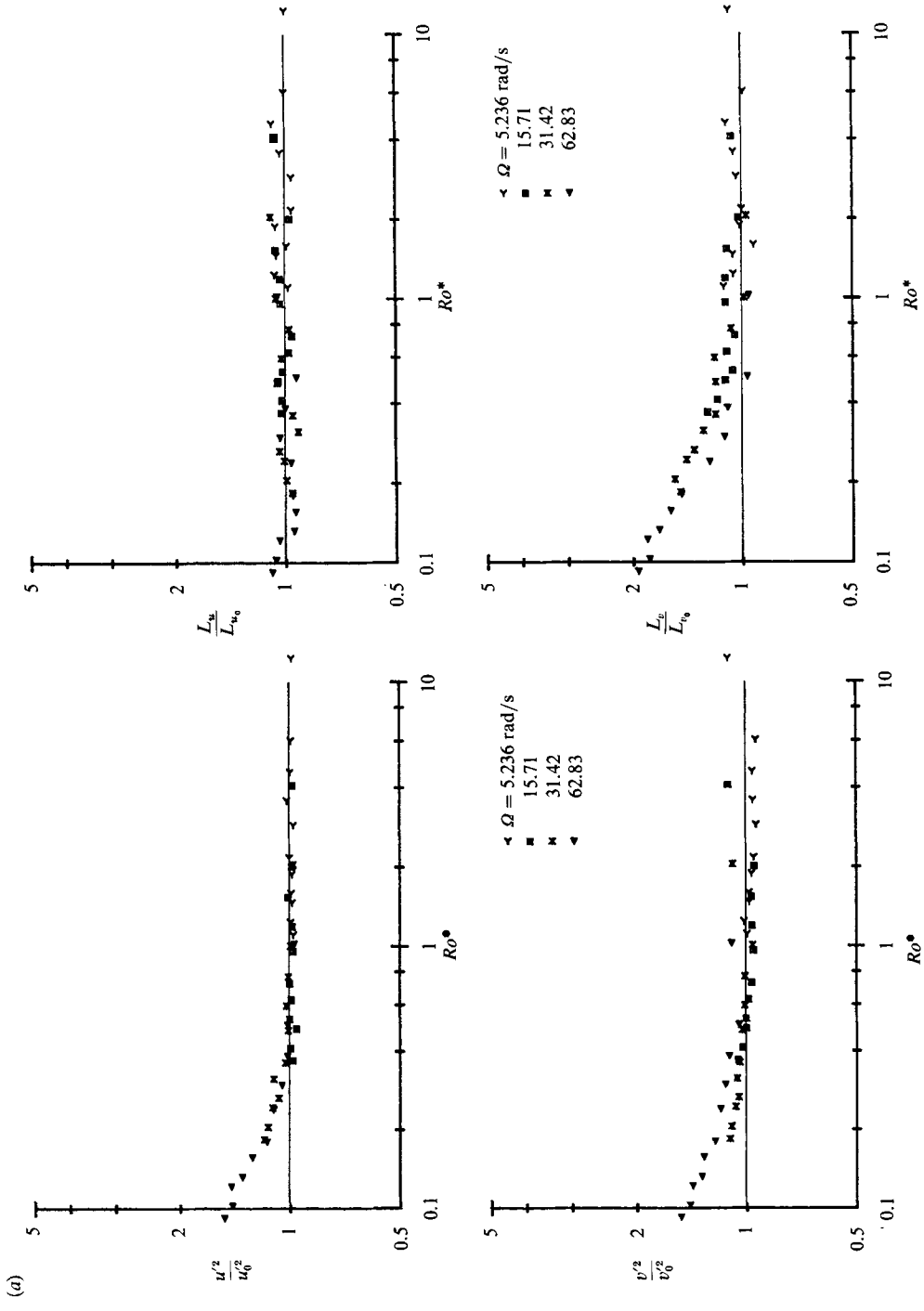


FIGURE 12(*a*). For caption see page 25.

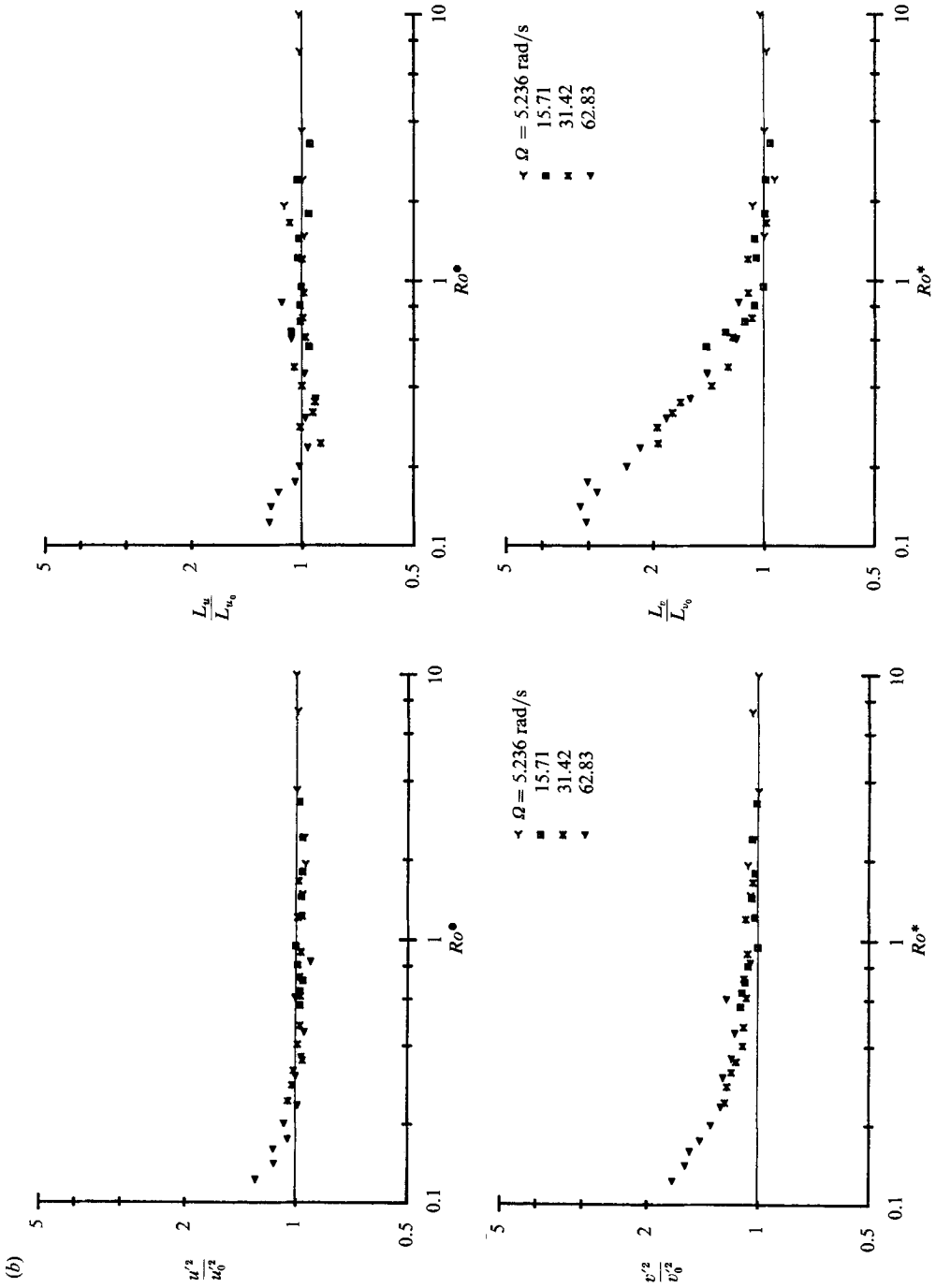
(b)
$\frac{u'^2}{u_0'^2}$
$\frac{L_u}{L_{u_0}}$
$\frac{v'^2}{v_0'^2}$
$\frac{L_v}{L_{v_0}}$
$Ro^*$
$\Omega = 5.236$ rad/s
15.71
31.42
62.83
5
2
1
0.5
0.1
10

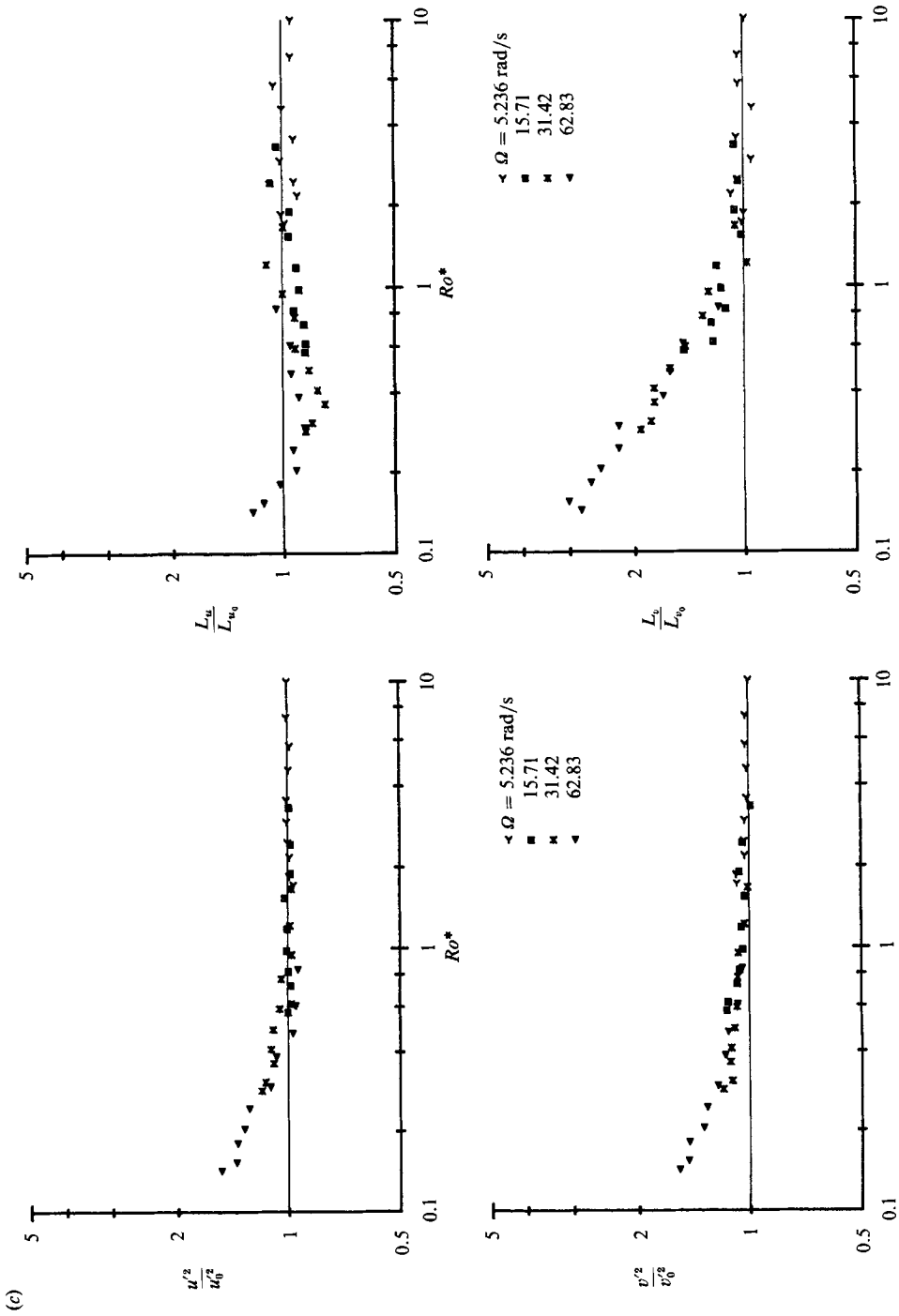


FIGURE 12. Normal stresses and integral lengthscales, normalized by the corresponding values at $\Omega = 0$, versus the 'fictitious' Rossby number $Ro^*$: (*a*) $M = 10$ mm, (*b*) $M = 15$ mm, (*c*) $M = 20$ mm.

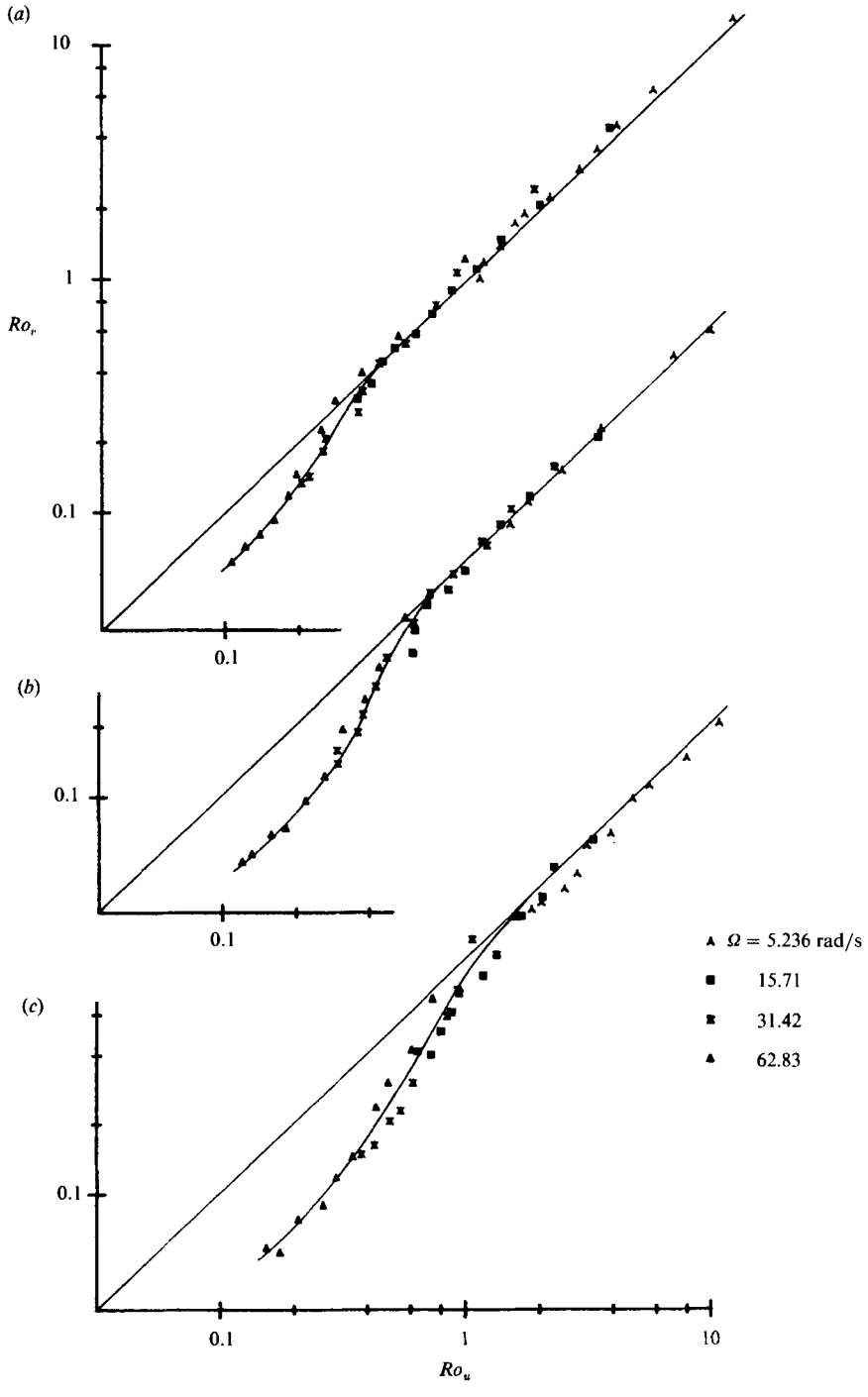


FIGURE 13. Rossby number $Ro_v$ versus Rossby number $Ro_u$: (a) $M = 10$ mm, (b) $M = 15$ mm, (c) $M = 20$ mm.

Finally, we tried to correlate these last results. To do so, we defined a 'fictitious' Rossby number defined as in (3.7) but with values calculated from the data without rotation:

$$Ro^* = \frac{\tau_\Omega}{\tau^*} \quad \text{with } \tau^* = \tau_u \approx \tau_v \quad \text{at } \Omega = 0. \tag{3.8}$$

$Ro^*$ is equivalent to the Rossby number $Ro_q$ calculated in §2.1 for the determination of the experimental configurations. It is like an 'external' parameter which is not affected by the rotation itself. If rotation had no effect on $\tau_u$ and $\tau_v$, for instance, $Ro_u$ and $Ro_v$ would still have the same value as $Ro^*$. But in reality, changes are expected for $Ro^* < 1$.

The Rossby numbers $Ro_u$ and $Ro_v$ have been plotted versus $Ro^*$ in figure 11. A rather good correlation is obtained even for $Ro^* < 1$. For $Ro^* > 1$, rotation effects do not exist and $Ro_u, Ro_v$, coincide with their fictitious values. For $Ro^* < 1$, $Ro_v$ departs from the diagonal and decays according to a particular power law whereas only a slight change can be detected on $Ro_u$. The 'transitional' values of the Rossby numbers which determine the limit between the two regimes are 0.6, 0.8 and 1.0 for $M = 10$, 15 and 20 mm, respectively.

Figure 11 summarizes the main information that has been inferred up to now from the experiment: rotation primarily affects the dynamics of the transverse part of the fluctuating field by increasing the time $\tau_v$ which characterizes the decay process of this component; that of the axial component is poorly affected; these mechanisms are triggered when the macroscopic Rossby numbers ($Ro_u$ or $Ro_v$) are less than unity; the 'transitional' value of the Rossby numbers associated with this change of regime seems to decrease with the mesh size; each regime apart from this transition can be characterized by means of particular power laws.

This ability of $Ro^*$ to correlate the various results is illustrated in figure 12, which shows $u'^2$, $v'^2$ and $L_u$, $L_v$, normalized by their corresponding values without rotation, as functions of $Ro^*$. Figure 12 (*a–c*) shows the results for each of the three grid mesh sizes.

The correlations are quite satisfactory. The increase of $v'^2(\Omega \neq 0)/v'^2(\Omega = 0)$ and of $L_v(\Omega \neq 0)/L_v(\Omega = 0)$ do correspond to the 'transitional' Rossby numbers (arrows in figure 11). Note that for the smallest value of $Ro^*$ and for $M = 15$ or 20 mm, $L_v$ can reach about 2.5 times its corresponding value without rotation.

As a conclusion, the fictitious Rossby number based on the reference flows at $\Omega = 0$ seems to be a relevant correlating parameter to describe the experiment.

Another interesting correlation is obtained by plotting $Ro_v$ as a function of $Ro_u$. The result is shown in figure 13. In accordance with the previous figure, a departure from an initial 'quasi-isotropic' relation $Ro_u \approx Ro_v$ is identified for a particular value of these parameters; this value increases with the mesh size; the rotation-dominated regime corresponds to a decrease of $Ro_v$ with respect to $Ro_u$. Moreover, this representation suggests the existence, at the smaller Rossby numbers, of an 'asymptoptic' regime corresponding to a power law of the type $Ro_u = (Ro_v)^n$, where the exponent $n$ is an increasing function of $x/M$.

## 4. Comparison with the experiment of Wigeland & Nagib

### 4.1. *Conclusions of the WN experiment*

The different configurations adopted by WN correspond to the parameters in table 4.

The main conclusions of WN are the following:

$U$ (m/s): 6, 9, 15
$M$ (mm): 2.54, 3.9, 6.25
$\Omega$ (rad/s): 6, 20, 40, 60, 80

TABLE 4. Experimental parameters for the WN experiment

(i) Except for certain configurations, rotation slows the decay of the kinetic energy $q^2$;

(ii) the slowing down of the decay of $q^2$ is primarily due to the reduction of that of $v'^2$;

(iii) this phenomenon is associated with a faster increase of the transverse integral scale $L_v$, and the axial scale $L_u$ is less affected;

(iv) when $q^2$ decays faster in the presence of rotation, mechanisms (ii) and (iii) are reversed;

(v) the dimensionless parameter $\Omega t = \Omega x/U$ characterizes changes in the structure of turbulence; the value $\Omega t/2\pi = 0.2$ plays a special role;

(vi) the parameter $M/U$ seems to have some influence: when $M/U < 0.001$ s, $q^2$ decays slower than in the absence of rotation, and the values of $q^2$ can be correlated by means of the parameter

$$\phi = \frac{\Omega t}{2\pi}\frac{U}{M} = \frac{\Omega x}{2\pi M}, \tag{4.1}$$

which scales as a frequency; when $M/U > 0.001$ s, and for the lowest values of $\Omega$ ($\Omega < 50$ rad/s), $q^2$ decays faster.

These conclusions will now be discussed in light of the present experiment.

### 4.2. *Reynolds stress components*

Results reported in figure 14 are calculated from the data given in WN for $U = 6$ m/s and $M = 3.9$ mm. This case gives a good illustration of the behaviour of the normal Reynolds stresses in the WN experiment.

Here, $M/U = 0.000\,65$ s and, accordingly to conclusion (vi) quoted in the previous section, $q^2$ must decay slower in the presence of rotation. This is true except for the smaller value of $\Omega$. Discarding this case, one sees from figure 14($b$) and ($c$) that the slowing down of the decay of $q^2$ is in fact due to the decay of $v'^2$. This is in accordance with conclusion (ii). However, figure 14($b$) shows that the decay of the axial component $u'^2$ increases. This partly counterbalances the first effect on $v'^2$. The same tendency, but even less pronounced, can be detected in our results in figure 6.

This particular aspect was not contained in the conclusions of the WN report, but in our opinion this is an important characteristic of this experiment. In particular, it can explain the role of the dimensional parameter $\Omega t/2\pi$ as noted in conclusion (v). This point will be developed in §5.

### 4.3. *Lengthscales*

Figure 15 shows the lengthscale variation corresponding to the same configuration as before.

The authors have calculated these quantities from the time correlations, using a numerical technique based on successive block averaging in order to smooth the tail of this function. The result is more or less equivalent to the modifications we made in order to treat the low-frequency range of the power spectral densities.

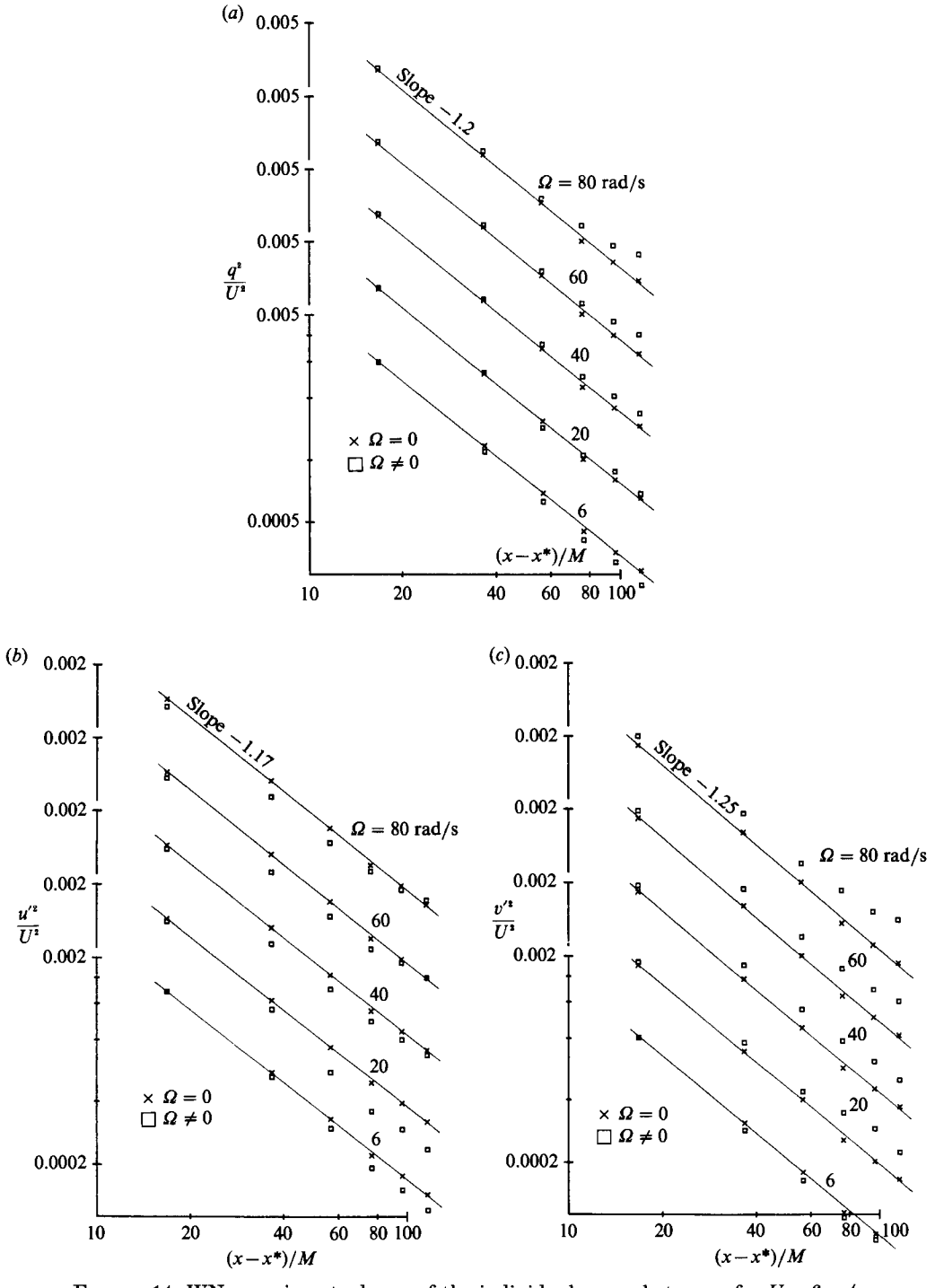


FIGURE 14. WN experiment: decay of the individual normal stresses for $U = 6$ m/s, $M = 3.9$ mm and various $\Omega$.

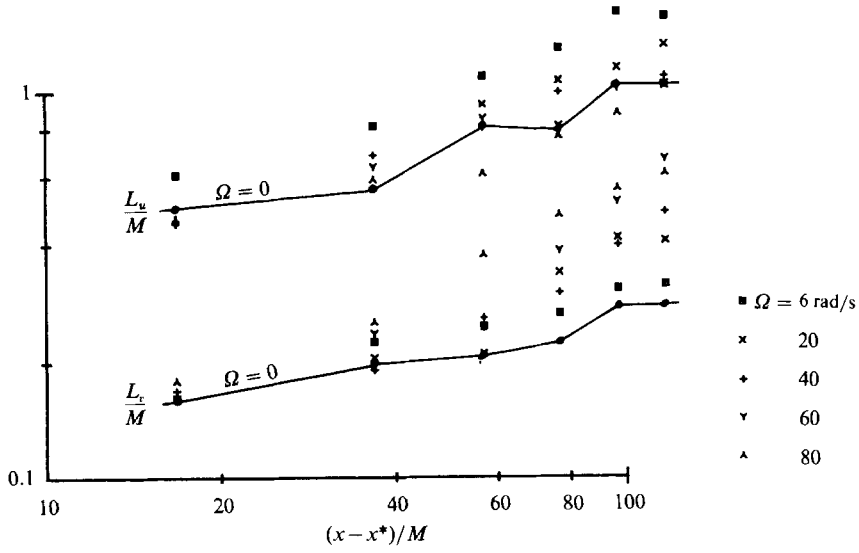


FIGURE 15. WN experiment: evolution of the integral lengthscales for $U = 6$ m/s, $M = 3.9$ mm and various $\Omega$.

Except again for $\Omega = 6$ rad/s, the accordance with our experiment is qualitatively fairly good. Both experiments are thus in accordance concerning conclusion (iii). But contrary to figure 9, no particular power laws can be detected in the WN results.

### 4.4. *Correlating parameters*

Concerning now the role of $M/U$ and that of the frequency $\phi$ defined in (4.1), with regard to conclusion (vi), WN advised further experimentation, with $M/U > 0.001$ s.

Our experiments, where $M/U = 0.0010$, 0.0015 and 0.0020 s respectively for $M = 10$, 15 and 20 mm fulfil this condition. However, the decay of the kinetic energy is never accelerated whatever the rotation rate (see figure 4).

Contrary to the macroscopic Rossby numbers used in the present study the parameter $\phi$ has no evident physical meaning. Figure 16(*a*) shows a cluster of values of $q^2$ using the same representation as WN. A figure of this type was used as a basis for conclusion (vi). Figure 16(*b*) shows the same quantities versus the Rossby number $Ro^*$ we introduced in §3.5. Here $Ro^*$ is taken equal to $\frac{1}{2}(Ro_u^* + Ro_v^*)$, owing to the fact that in the WN experiment the characteristic times $\tau_u$ and $\tau_v$ are not equal (see (3.7) and (3.8)).

The correlations are not very good in either case, but the second is not worse than the first. On figure 16(*b*), the rise in $q^2(\Omega \neq 0)/q^2(\Omega = 0)$ seems to be associated with values of $Ro^*$ less than unity.

This last curve is evidently easier to interpret. In fact, in the WN report the frequency $\phi$ only correlated $q^2$. The variations of these functions are slight and $\phi$ is unable to correlate other parameters such as, for instance, the integral lengthscales.

Figure 17 shows a correlation of $Ro_u$ and $Ro_v$ versus $Ro_u^*$ and $Ro_v^*$ for the same experimental configuration discussed in the two previous sections. The correlations are not very good, owing to the dispersion of the experimental values (mainly the lengthscales) and to the errors introduced during the determination of these values from the figures of the report. However, the same tendency appears in figure 11, with

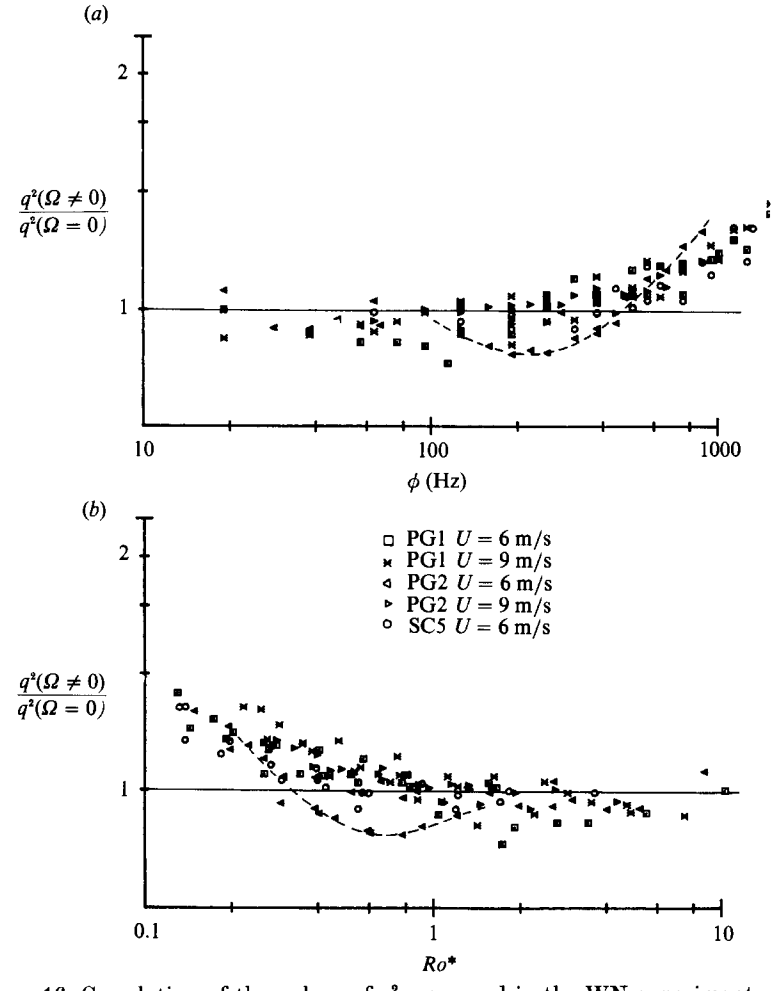


FIGURE 16. Correlation of the values of $q^2$ measured in the WN experiment: (*a*) versus the frequency $\phi$, (*b*) versus $Ro^*$.

a faster decrease of $Ro_v$ for values smaller than unity. We reach the same conclusions from certain other cases we investigated.

## 5. Displaced particle analysis

The next two sections will present theoretical developments based on a spectral approach. Before going further in this direction, a simple 'displaced particle' argument may already bring useful information on a few of the basic mechanisms responsible for the phenomena observed in the experiment.

A displaced particle argument leads, for instance, to a simple physical description of the stabilizing or destabilizing role of rotation in a rotating shear flow (Tritton & Davies 1981). This approach can also help to identify the relevant lengthscales for the modelling of turbulent shear flows in the presence of a body force (Hunt, Stretch & Britter 1988). In the case of a rotating grid generated turbulence the argument can be stated as follows.

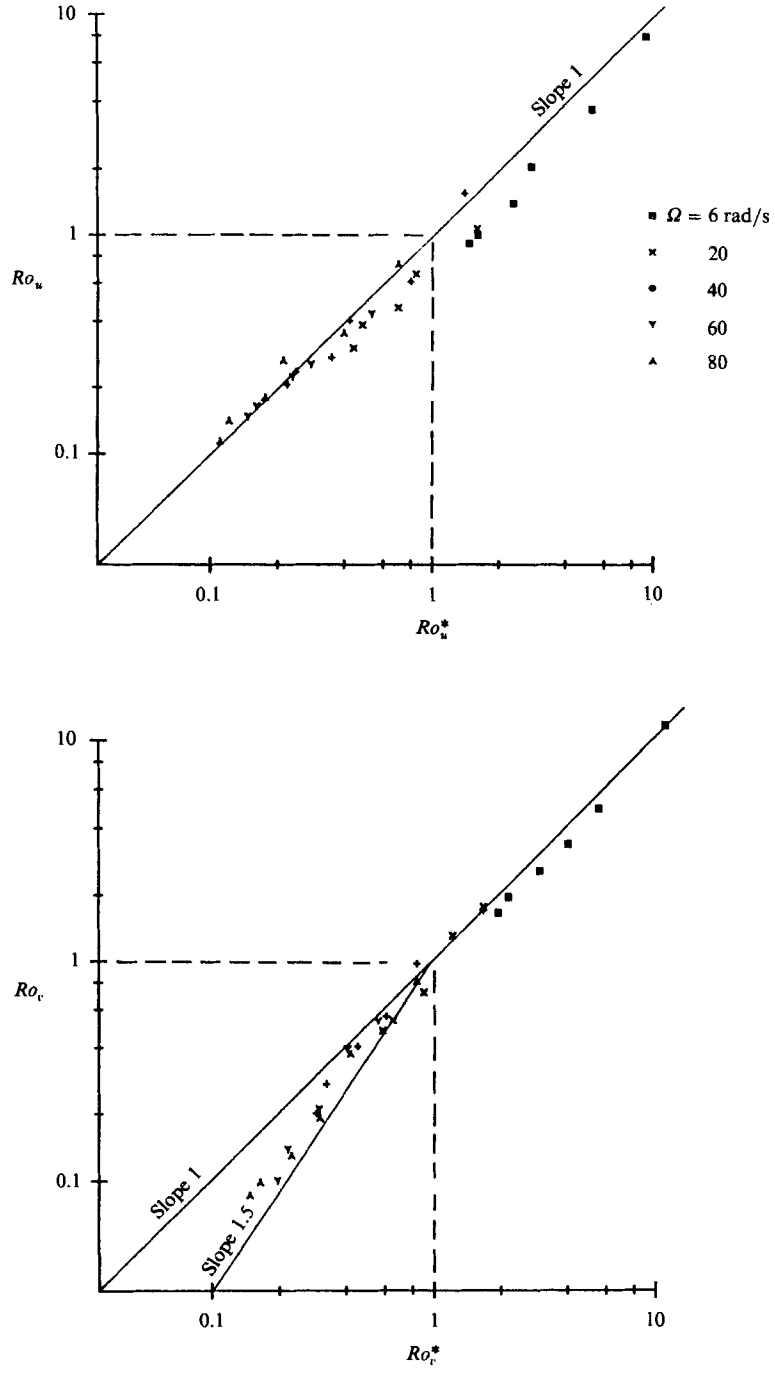


FIGURE 17. WN experiment: Rossby numbers $Ro_u, Ro_v$ versus the 'fictitious' Rossby numbers $Ro_u^*$ and $Ro_v^*$ for $U = 6$ m/s, $M = 3.9$ mm.

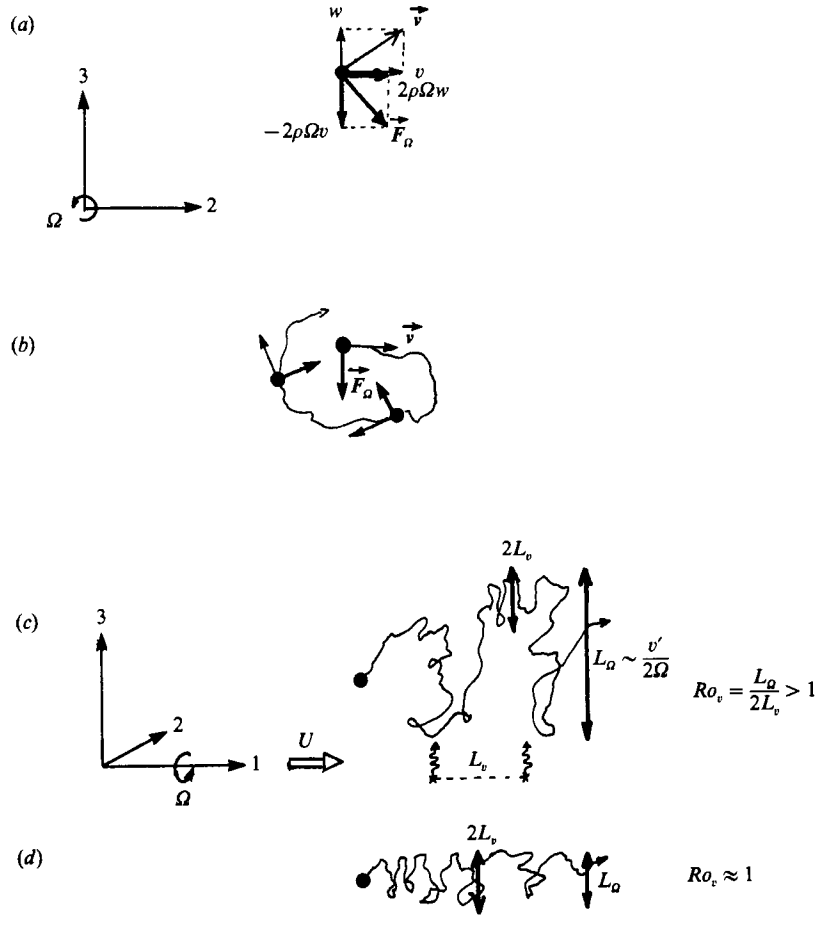


FIGURE 18. Sketch of the influence of the Coriolis force $f_\Omega$ on a displaced fluid element: Coriolis force components, (*a*); typical trajectory of the fluid particle in the plane normal to the rotation axis, (*b*); typical trajectories in the presence of an axial mean velocity in high, (*c*), and low, (*d*), Rossby flows with corresponding dissipation ($2L_v$) and diffusion ($L_\Omega$) lengthscales.

The flow is considered in a moving frame rotating at a rate $\Omega$. As sketched in figure 18(*a*), a fluid element is displaced in the plane normal to the rotation axis (axis 1) with a given velocity $\boldsymbol{v}(0, v, w)$, and is subjected to a Coriolis force of components $\boldsymbol{f}_\Omega(0, +2\Omega\rho w, -2\Omega\rho v)$. The particle has a circular trajectory (figure 18*b*). Thus, the Coriolis force tends to inhibit the transversal (normal to $\boldsymbol{\Omega}$) movements of the fluid element, in a similar way that the buoyancy force damps the vertical displacements in a stably stratified turbulent flow. Note that in the stratification case an exchange occurs between the potential energy and the vertical kinetic energy, whereas in the rotation case the reduction of transverse displacements has no consequence, *a priori*, on the energy of the transversal fluctuations.

The above arguments suggest $L_\Omega \sim (v'^2 + w'^2)^{\frac{1}{2}}/2\Omega \approx v'/2\Omega$ as a relevant lengthscale for the mean transverse displacement of the fluid elements. This means that most fluid elements are displaced laterally within a distance of order $v'/2\Omega$ (in a stratified flow, one can similarly use the buoyancy lengthscale as $L_N \approx w'/N$, where $N$ is the buoyancy frequency, to characterize the mean vertical displacement of the fluid elements (see Hunt *et al.* 1988)). $L_\Omega$ can also be interpreted as the characteristic

scale of the eddies whose vorticity ($\approx v'/L_\Omega$) is proportional to the mean vorticity of the flow ($2\Omega$). One can simply call the scale $L_\Omega$, the 'Coriolis lengthscale'. Another possibility could be 'radius of gyration' in line with the usage in plasma physics for a particle in a magnetic field.

The second relevant lengthscale in our flow is an integral lengthscale, e.g. $2L_v$. This scale is initially proportional to the mesh size of the grid. In the absence of rotation, $2L_v$ determines the dissipation rate of the turbulence. When background rotation is added, the two lengthscales are 'in competition' and their ratio is the Rossby number $Ro_v$ (see (3.7)).

The experiment shows that a rotation-dominated regime associated with a transverse structure of the flow (increase of $L_v$) and a modification of the dissipation occurs when $Ro_v < 1$, that is when $L_\Omega < 2L_v$. Within the frame of the present analysis, this means that rotation affects the turbulence when the energy containing eddies become sufficiently large to be influenced by the 'transverse confinement' imposed by the Coriolis force.

The arguments lead also to the conclusion that the lengthscales involving only the axial fluctuations, as for example the integral lengthscale $L_u$, are likely to be less affected by the Coriolis force which is restricted to the transversal plane (any effect on $L_u$ must be attributed to the pressure which connects the transverse and axial movements). This is confirmed by the experiment.

As sketched in figure 18 ($c, d$), the addition of a mean axial flow along the rotation axis leads, in a sufficiently low-Rossby-number case ($d$), to axially elongated trajectories similar to columnar structures. In such a flow, one can effectively expect an increase of $L_v$ which measures the mean correlation length in the axial direction of instantaneous transversal fluctuations. Correlation lengths of transverse fluctuations in the transversal direction, whose measurement would necessitate the use of two probes, have not been measured. The above argument also suggests an increase of this scale. Such an increase has been demonstrated by the numerical simulation of Bardina *et al.* (1985) and it has also been found in the EDQNM results of Cambon & Jacquin (1989) (however, these various computations have shown that the scales $L_{ii,1}$, $i = 2, 3$, are the most sensitive to rotation).

The main weakness of this argument is to ignore the impact of the fluctuating pressure. As it will be shown in the next two sections, spectral analysis is a convenient tool to investigate rigorously the role of (at least part of) the pressure terms in the basic equations.

## 6. Linear regime

In this section, we will discuss possible linear interpretations of some of the above experimental results, especially the possible impact of the inertial wave regime. This concept will first be recalled in §6.1. Sections 7 and 8 will be devoted to the influence of these waves on the Reynolds stresses and to their interaction with the solid boundaries of the apparatus.

### 6.1. *Inertial waves*

Inertial waves characterize the way perturbations propagate in a rotating fluid. They correspond to the linear solution of the Navier–Stokes equations in a rotating reference frame (see e.g. Greenspan 1968):

$$\frac{\partial}{\partial t}\boldsymbol{u}(\boldsymbol{x},t)+2\boldsymbol{\Omega}\times\boldsymbol{u}(\boldsymbol{x},t)+\frac{1}{\rho}\boldsymbol{\nabla}p+\nu\boldsymbol{\nabla}\times(\boldsymbol{\nabla}\times\boldsymbol{u}(\boldsymbol{x}))=\boldsymbol{u}(\boldsymbol{x},t)\,(\boldsymbol{\nabla}\boldsymbol{u}(\boldsymbol{x},t)). \tag{6.1}$$

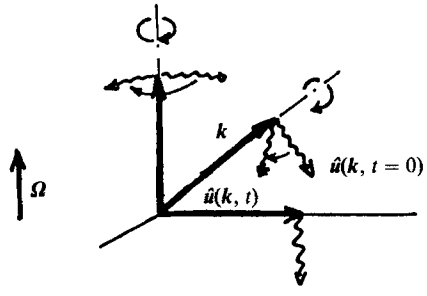


FIGURE 19. Rotation of the initial spectrum $\hat{\boldsymbol{u}}(\boldsymbol{k}, t=0)$ in the plane normal to $\boldsymbol{k}$.

If we neglect the right-hand side of this equation, the solution is a wave regime of the kind

$$\boldsymbol{u}(\boldsymbol{x},t) = \mathrm{Re}\{\hat{\boldsymbol{u}}_0(\boldsymbol{k}) \exp\{-i(\boldsymbol{k}\cdot\boldsymbol{x} \pm \omega(\boldsymbol{k})\, t)\} \exp(-\nu k^2 t)\}, \tag{6.2}$$

with a phase speed equal to

$$\frac{\omega(\boldsymbol{k})}{k} = \frac{2\boldsymbol{\Omega}\cdot\boldsymbol{k}}{k^2}. \tag{6.3}$$

Let $\hat{\boldsymbol{u}}(\boldsymbol{k})$ denote the spectrum of $\boldsymbol{u}(\boldsymbol{x})$:

$$\hat{\boldsymbol{u}}(\boldsymbol{k},t) = \frac{1}{(2\pi)^3} \int_{R^3} \boldsymbol{u}(\boldsymbol{x},t) \exp(-i\boldsymbol{k}\cdot\boldsymbol{x})\, \mathrm{d}\boldsymbol{x}. \tag{6.4}$$

For an incompressible flow: $\boldsymbol{k}\cdot\hat{\boldsymbol{u}}(\boldsymbol{k}) = 0$. The linear spectrum $\hat{\boldsymbol{u}}(\boldsymbol{k},t)$ is written (Cambon & Jacquin 1989):

$$\hat{\boldsymbol{u}}(\boldsymbol{k},t) = \boldsymbol{R}\left(\frac{\boldsymbol{k}}{k}, \frac{2\boldsymbol{\Omega}\cdot\boldsymbol{k}}{k} t\right) \exp(-\nu k^2 t)\, \hat{\boldsymbol{u}}(\boldsymbol{k}, t=0), \tag{6.5}$$

where $\boldsymbol{R}(\boldsymbol{k}/k, \phi)$ denotes the rotation matrix having $\phi$ for its angle and $\boldsymbol{k}$ for its axis. The anisotropic propagation of the inertial waves in physical space corresponds in spectral space to a differential rotation of the initial spectrum $\hat{\boldsymbol{u}}(\boldsymbol{k}, t=0)$ in the plane normal to $\boldsymbol{k}$, with a rate $2\boldsymbol{\Omega}\cdot\boldsymbol{k}/k$. As sketched in figure 19, this rotation is maximum for $\boldsymbol{k}$ parallel to $\boldsymbol{\Omega}$, and null for $\boldsymbol{k}$ normal to $\boldsymbol{\Omega}$.

The inertial waves are dispersive. Their phase speed (6.3) depends on the magnitude of the wave vector, but also on its orientation. This 'anisotropic dispersivity' plays a fundamental role with regard to the dynamics of rotating fluids.

### 6.2. *Inertial waves in an homogeneous flow*

The simultaneous correlation between two spectra $\hat{\boldsymbol{u}}(\boldsymbol{k})$

$$\langle \hat{\boldsymbol{u}}^*(\boldsymbol{p},t)\, \hat{\boldsymbol{u}}(\boldsymbol{k},t) \rangle = \hat{\boldsymbol{U}}(\boldsymbol{k},t)\, \delta(\boldsymbol{k}-\boldsymbol{p}) \tag{6.6}$$

defines the second-order spectral tensor. The Reynolds stress tensor, $U_{ij}(t)$, corresponds to an integration over $\boldsymbol{k}$ of $\hat{\boldsymbol{U}}(\boldsymbol{k},t)$:

$$U_{ij}(t) = \langle u_i(\boldsymbol{x},t)\, u_j(\boldsymbol{x},t) \rangle = \int_{R^3} \hat{U}_{ij}(\boldsymbol{k},t)\, \mathrm{d}\boldsymbol{k}. \tag{6.7}$$

The kinetic energy reads

$$\tfrac{1}{2} q^2(t) = \tfrac{1}{2} \langle u_i(\boldsymbol{x},t)\, u_i(\boldsymbol{x},t) \rangle = \tfrac{1}{2} \int_{R^3} \hat{U}_{ii}(\boldsymbol{k},t)\, \mathrm{d}\boldsymbol{k}. \tag{6.8}$$

In this section, one considers a superposition of non-interacting inertial waves. From (6.5) we get

$$\hat{\boldsymbol{U}}(\boldsymbol{k},t)=\boldsymbol{R}\left(\frac{\boldsymbol{k}}{k},\frac{2\boldsymbol{\Omega}\cdot\boldsymbol{k}}{k}t\right)\hat{\boldsymbol{U}}(\boldsymbol{k},t=0)\,\boldsymbol{R}\left(\frac{\boldsymbol{k}}{k},-\frac{2\boldsymbol{\Omega}\cdot\boldsymbol{k}}{k}t\right)\exp(-2\nu k^2 t), \tag{6.9}$$

with $\boldsymbol{k}\cdot\hat{\boldsymbol{U}}(\boldsymbol{k})=0$ for an incompressible flow. From (6.9) one sees that the linear effect of rotation on $\hat{\boldsymbol{U}}$ is analogous to its effect on $\hat{\boldsymbol{u}}$: it corresponds to a differential rotation of the initial tensor $\hat{\boldsymbol{U}}(\boldsymbol{k},t=0)$ in the plane normal to $\boldsymbol{k}$ with a rate $4(\boldsymbol{\Omega}\cdot\boldsymbol{k}/k)\,t$. The kinetic energy (6.8) is only influenced by viscosity.

If the fluctuating field is initially (three-dimensional) isotropic, with:

$$U_{ij}(\boldsymbol{k},t=0)=\frac{E_0(k)}{4\pi k^2}\left(\delta_{ij}-\frac{k_i k_j}{k^2}\right), \tag{6.10}$$

from (6.9): $$\hat{\boldsymbol{U}}(\boldsymbol{k},t)=\hat{\boldsymbol{U}}(\boldsymbol{k},t=0)\exp(-2\nu k^2 t), \tag{6.11}$$

then, isotropy is conserved.

Let us consider now the case of an initially non-isotropic fluctuating field. Through (6.9) the eigen directions of $\hat{\boldsymbol{U}}(\boldsymbol{k},t=0)$ will be rotated in a way which depends on the orientation of $\boldsymbol{k}$. In accordance with (6.7), the Reynolds stress tensor $U_{ij}(t)$ which corresponds to a three-dimensional integration of $\hat{\boldsymbol{U}}(\boldsymbol{k},t)$ over $\boldsymbol{k}$, will thus entirely depend on the precise distribution of $\hat{\boldsymbol{U}}(\boldsymbol{k},t=0)$.

In a rotating frame, the equations of the Reynolds stress tensor (with $\boldsymbol{\Omega}$ parallel to the axis 1) are

$$\left.\begin{aligned}
\frac{\partial}{\partial t}\langle u_1^2\rangle &= \frac{2}{\rho}\left\langle p\frac{\partial u_1}{\partial x_1}\right\rangle-2\nu\left\langle\frac{\partial u_1}{\partial x_k}\frac{\partial u_1}{\partial x_k}\right\rangle,\\
\frac{\partial}{\partial t}\langle u_2^2\rangle &= \underline{-4\Omega\langle u_2 u_3\rangle}+\frac{2}{\rho}\left\langle p\frac{\partial u_3}{\partial x_2}\right\rangle-2\nu\left\langle\frac{\partial u_2}{\partial x_k}\frac{\partial u_2}{\partial x_k}\right\rangle,\\
\frac{\partial}{\partial t}\langle u_3^2\rangle &= \underline{4\Omega\langle u_2 u_3\rangle}+\frac{2}{\rho}\left\langle p\frac{\partial u_3}{\partial x_3}\right\rangle-2\nu\left\langle\frac{\partial u_3}{\partial x_k}\frac{\partial u_3}{\partial x_k}\right\rangle,\\
\frac{\partial}{\partial t}\langle u_2 u_3\rangle &= \underline{2\Omega(\langle u_2^2\rangle-\langle u_3^2\rangle)}-\frac{1}{\rho}\left\langle p\frac{\partial u_2}{\partial x_3}\right\rangle-\frac{1}{\rho}\left\langle p\frac{\partial u_3}{\partial x_2}\right\rangle\\
&\quad -2\nu\left\langle\frac{\partial u_2}{\partial x_k}\frac{\partial u_3}{\partial x_k}\right\rangle.
\end{aligned}\right\} \tag{6.12}$$

In the second part of these equations, the underlined terms are the 'Coriolis terms' (which are redistribution terms). One then identifies the 'pressure terms' and the 'dissipation terms'.

The integral over $\boldsymbol{k}$ of (6.9) is the solution to this system if we neglect the nonlinear part of the pressure terms (the 'slow part' of the pressure strain correlations).

The strong sensitivity of the linear solution of rotation to the initial state has been illustrated by Townsend (1976), Itsweire *et al.* (1979), Jacquin *et al.* (1986) and Cambon & Jacquin (1987). In these references, the initial states were obtained by applying a rapid distortion to an isotropic spectrum. The first two authors considered the case of a plane distortion and the second, that of axisymmetric convergence and divergence. In the three last references, the tensor $\hat{\boldsymbol{U}}(\boldsymbol{k},t=0)$ at the end of these 'devices' was determined by means of Craya's spectral method (1958). These conditions were then injected in the linear solution (6.9).

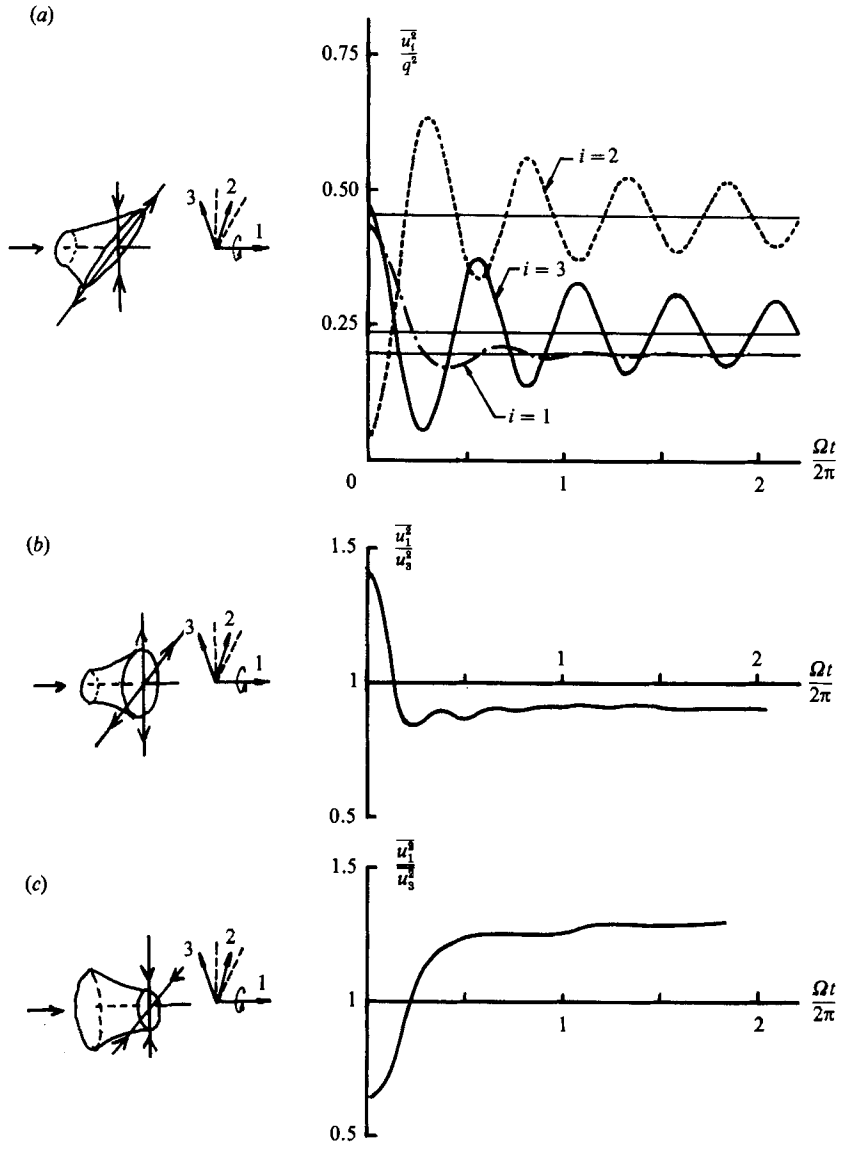


FIGURE 20. Linear evolution of the normal stresses under solid body rotation of various non-isotropic initial conditions: (*a*) plane distortion (Itsweire *et al.* 1981); (*b*) dilatation; (*c*) contraction (Jacquin *et al.* 1986).

As an illustration, figure 20 shows the corresponding variation of the Reynolds stress components versus the parameter ($\Omega t$) for the three different initial states.

In the case of figure 20(*a*) (plane distortion) the oscillations of the components normal to $\boldsymbol{\Omega}$ are due to the action of the underlined terms of (6.12). These terms are null for the two other cases (equidistribution of the transverse components). In all three cases, energy is redistributed between the transverse and the axial components. This can only be due to the (rapid) pressure action. This redistribution, as well as the oscillations of the normal components in figure 20(*a*), are rapidly damped. This is again a consequence of pressure effects. The asymptotic anisotropy depends entirely on the initial anisotropy. For example, a 'cigar' type Reynolds tensor (figure 20(*b*),

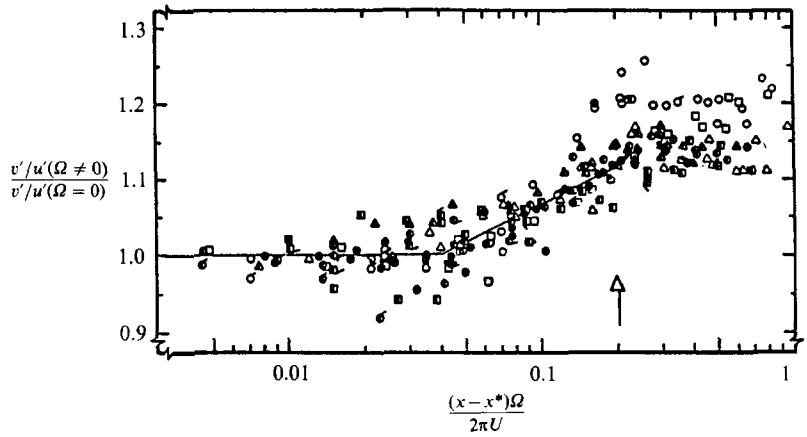


FIGURE 21. WN experiment: Correlation of $v'/u'$ versus $\Omega(x-x^*)/2\pi U$ for all configurations and all rotation rates (figure from Wigeland & Nagib, 1978).

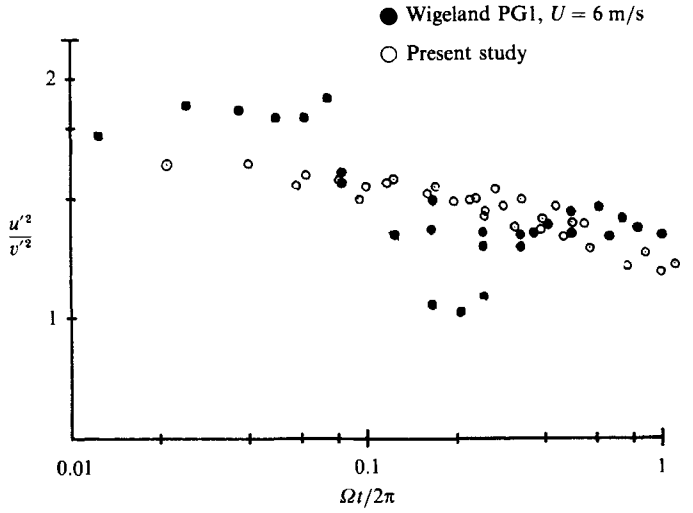


FIGURE 22. Evolution of $u'/v'$. WN experiment: $U = 6$ m/s, $M = 3.9$ mm; present experiment: $U = 10$ m/s, $M = 15$ mm.

$\overline{u_2^2} \approx \overline{u_3^2} < \overline{u_1^2}$) becomes a 'pancake' type, whereas a 'pancake' type Reynolds tensor (figure 20(*c*), $\overline{u_1^2} < \overline{u_2^2} \approx \overline{u_3^2}$) becomes a 'cigar' type.

These linear effects of rotation can play an important role in experiments where pure isotropic conditions are rarely achieved.

Figure 21 is what supports conclusion (v) in WN. It shows the variation of the 'anisotropic parameter' $v'/u'$ normalized by the corresponding values obtained for $\Omega = 0$, for all the configurations of table 4, versus $\Omega(x-x^*)/2\pi U$. If we neglect the influence of the origin $x^*$ for sufficiently large values of $x/M$, this parameter is equivalent to $\Omega t/2\pi$. In the absence of rotation, $v'/u'$ was about 0.74 so that figure 21 shows that this initial anisotropy decreases as $\Omega t/2\pi$ increases. When the latter reaches about 0.2, then a broad plateau is obtained. As in figure 20(*c*), a quarter revolution ($\Omega t/2\pi = 0.25$) characterizes the end of the linear influence of rotation.

This behaviour is also illustrated in figure 22 for the particular configuration which has been detailed in §4. Our experimental points corresponding to $M = 15$ mm are superimposed in this figure. In accordance with figure 7, this case is the only one with any significant changes in $v'/u'$. Here $t$ denotes the time elapsed since the grid. In the WN experiment, a rapid return towards isotropy is observed up to $\Omega t/2\pi \approx 0.2$, whereas our own results show a gradual attenuation of anisotropy.

Thus, the strong damping of a high initial anisotropy in the WN experiment could be fairly attributed to linear effects similar to those of figure 20(*c*). However, contrary to the pure linear solution shown in this figure, the anisotropy is never inverted in figures 21 and 22. Nonlinear damping seems to be the reason for this smoother behaviour. This has been confirmed by calculations with an EDQNM model for the nonlinear terms (Jacquin *et al.* 1986; Cambon & Jacquin 1987).

In conclusion, if the turbulence is initially non-isotropic, the impact of inertial waves can be spectacular: the variation of the Reynolds stress tensor is strongly affected by the linear part of the pressure–strain correlation which reflects the inertial wave effect. These effects are transitory and the final anisotropy depends entirely on the initial anisotropy. In the case of a grid-generated turbulence, with a 'cigar type' anisotropy, a quarter of a revolution seems to fix the end of these effects.

### 6.3. *Inertial waves propagating in a vessel*

As a consequence of their dispersivity, the inertial waves can transport the energy of the fluctuations, which can then be dissipated at the boundaries of an apparatus during multiple reflections.

Phillips (1963) gave a complete theory of this problem. This theory provides the basis for one of the most plausible interpretations Ibbetson and Tritton gave of their experiment. In Phillips' paper, the relevant parameters are introduced as follows.

The speed of energy transport by the inertial waves is given by the group velocity (see also Greenspan 1968):

$$\boldsymbol{c}_{\mathrm{g}}(\boldsymbol{k}) = \boldsymbol{\nabla}_{\boldsymbol{k}}(\omega(\boldsymbol{k})) = \boldsymbol{\alpha} \times \frac{2\boldsymbol{\Omega} \times \boldsymbol{\alpha}}{k}, \tag{6.13}$$

with $\boldsymbol{\alpha} = \boldsymbol{k}/k$, $\omega(\boldsymbol{k})$ being the pulsation defined in (6.3) and $\boldsymbol{\nabla}_{\boldsymbol{k}}$, the gradient in $\boldsymbol{k}$ space. Through (6.13) the energy is transferred at right angles with respect to $\boldsymbol{k}$ (the group speed is normal to the phase speed). If

$$e(\boldsymbol{k}, t) = \tfrac{1}{2}\langle \hat{u}_{\mathrm{i}}(\boldsymbol{k}, t)\, \hat{u}_{\mathrm{i}}(-\boldsymbol{k}, t)\rangle \tag{6.14}$$

denotes the energy of an inertial wave ($\boldsymbol{k}$) at instant $t$, Phillips showed that during a reflection on a boundary, $e(\boldsymbol{k}, t)$ is dissipated with a proportion of the order

$$\frac{\Delta e}{e}(\boldsymbol{k}) = \frac{e_{\mathrm{i}}(\boldsymbol{k}) - e_{\mathrm{r}}(\boldsymbol{k}')}{e_{\mathrm{i}}(\boldsymbol{k})} \sim E_K^{\frac{1}{2}} \tag{6.15}$$

where $\boldsymbol{k}$ and $\boldsymbol{k}'$ denote respectively the incident and the reflected wave, and

$$E_K = \frac{\nu K^2}{2\Omega} \tag{6.16}$$

is an Ekman number built on the wavenumber $K$ equal to the projection of $\boldsymbol{k}$ on the boundary. Through (6.13) and (6.15), the orientation of $\boldsymbol{k}$ and that of the boundary, with respect to $\boldsymbol{\Omega}$, must be both taken into account in order to deal with this

phenomenon (see Ibbetson & Tritton (1975) for more details on this point). However, ignoring this directional aspect of the problem and following Phillips one can retain the parameter

$$\frac{\Delta E(k)}{E(k)} = AE_k^{-\frac{1}{2}} = A\left(\frac{\nu k^2}{2\Omega}\right)^{\frac{1}{2}} \tag{6.17}$$

for characterizing the dissipation of the energy $E(k)$ of a wave $(k)$ (by multiple reflections with the boundaries of an apparatus). $E(k)$ denotes the integral of $e(\boldsymbol{k})$ on a spherical shell of radius $k$ and we have introduced a constant $A$ in order to take into account the directional aspects which have been neglected.

Ibbetson & Tritton have proposed a possible interpretation of their experiment by considering their flow as a superposition of non-interacting inertial waves. From Phillips' theory, they proposed an inertial model for the increasing decay of energy with rotation they observed in their experiment. For $E(k)$, the model reads:

$$\left\{\frac{\mathrm{d}}{\mathrm{d}t} + 2\nu k^2 + \frac{\Delta E}{E}(k)\frac{1}{\tau_t}\right\} E(k,t) = 0 \tag{6.18}$$

with the attenuation rate $(\Delta E/E)(k)$ defined in (6.17) and where the time

$$\tau_t = \frac{D}{c_g} \tag{6.19}$$

is the mean time of transit of a wave $(k)$ in a vessel whose characteristic size is $D$. Finally that leads to:

$$\left\{\frac{\mathrm{d}}{\mathrm{d}t} + 2\nu k^2 + AE_D^{\frac{1}{2}}2\Omega\right\} E(k,t) = 0, \tag{6.20}$$

where

$$E_D = \frac{\nu}{2\Omega D^2}.$$

An integration of (6.20) over $k$ leads to the following balance equation for the kinetic energy:

$$\frac{\mathrm{d}\frac{1}{2}q^2}{\mathrm{d}t} = -(\tau^{-1} + A\tau_s^{-1})\tfrac{1}{2}q^2, \tag{6.21}$$

where

$$\tau = \frac{\frac{1}{2}q^2}{\epsilon} \tag{6.22}$$

$$\tau_s = \frac{E_D^{-\frac{1}{2}}}{2\Omega} = \left(\frac{D^2}{2\nu\Omega}\right)^{\frac{1}{2}}. \tag{6.23}$$

The time $\tau_s$ characterizes the dissipation in the Ekman layers. $\tau_s$ defines also the spin-up time of the vessel.

From the two characteristic times $\tau$, $\tau_s$ and the rotation time

$$\tau_\Omega = (2\Omega)^{-1}, \tag{6.24}$$

one can deduce three relevant parameters: a Rossby number

$$Ro_q = \frac{\tau_\Omega}{\tau} = \frac{\epsilon}{q^2\Omega} \tag{6.25}$$

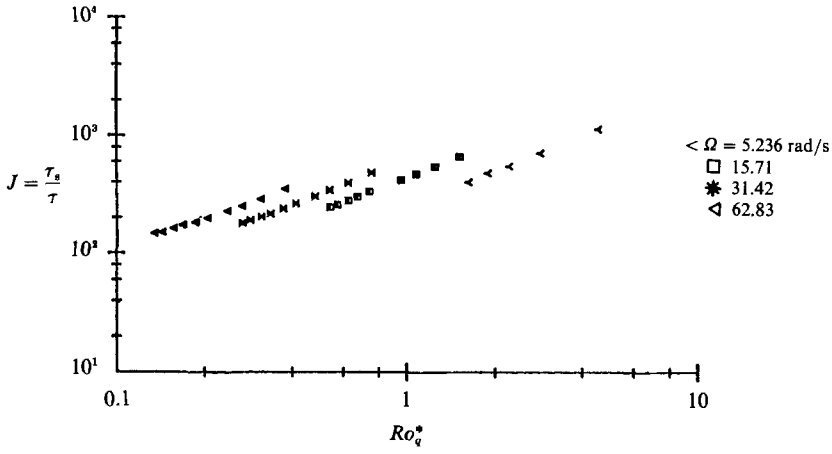


FIGURE 23. Parameter $J$ versus the 'fictitious' Rossby number for $M = 15$ mm.

which characterizes the balance between the rotation effects (whatever they be) and the dynamics of the fluctuating field; the Ekman number (its square root)

$$E_D^{\frac{1}{2}} = \frac{\tau_\Omega}{\tau_s} = \left(\frac{\nu}{2\Omega D^2}\right)^{\frac{1}{2}}, \tag{6.26}$$

which evaluates the relative importance of the Ekman dissipation with respect to other rotation effects on the flow; and the ratio between these two numbers

$$J = \frac{\tau_s}{\tau} = \frac{Ro_q}{E_D^{\frac{1}{2}}}, \tag{6.27}$$

which evaluates the influence of boundaries on the dynamics of the flow ($J$ was given by Ibbetson & Tritton in a different form by introducing the Reynolds number). An experiment where $Ro_q < E_D^{\frac{1}{2}}$ will be marked by important boundary effects and will thus be outside the frame of homogeneity.

In the experiment of Ibbetson & Tritton, when an increase of the decay of $\frac{1}{2}q^2$ with rotation was observed, the typical lowest values of $J$ were about ten. As proposed by these authors, such a high value could reflect the (neglected) directional aspects of the mechanisms.

$J$ has been determined in the present experiment. $\epsilon$, which enters into the definition of $Ro_q$, was calculated from relation (2.2) by a determination of an exponent $\alpha$ and an origin $x^*$ for each $M$ and $\Omega$ in the same way as for figure 4(*d*). Figure 23 shows the evolution of $J$ for $M = 15$ mm ($J$ is plotted versus a 'fictitious' Rossby number $Ro_q$ which has been determined from the results without rotation).

In figure 23, $J$ is greater than one hundred. The same order of magnitude is obtained for the two other grids. The same conclusion is reached from the WN results.

A conclusion is that boundary effects seemed negligible in these experiments which are thus valuable with regard to this particular homogeneity constraint.

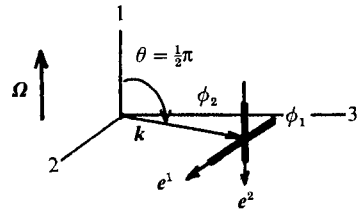


FIGURE 24. Representation of $\hat{\boldsymbol{U}}(\mathbf{k})$ in the plane $k_1 = 0$ through its eigenmodes $\phi_1$ and $\phi_2$ in the local frame ($\mathbf{e}^1 = (\mathbf{k}/k) \times (\boldsymbol{\Omega}/\Omega)$, $\mathbf{e}^2 = (\mathbf{k}/k) \times \mathbf{e}^1$).

## 7. Nonlinear effects and transition towards two-dimensional turbulence

The present experiment shows that the rotation effects are strongly anisotropic. The most significant illustration of this structuring is the behaviour of the characteristic times $\tau_u$ and $\tau_v$, or those of the corresponding macroscopic Rossby numbers $Ro_u$ and $Ro_v$. In this section we discuss the possible connections between these results and the problem of the transition towards two-dimensionality.

### 7.1. *Spectral formalism*

A full spectral formalism was developed by Cambon & Jacquin (1989) to deal with the anisotropic influence of rotation on nonlinear wave interactions. The full development of this theory is not necessary for our purposes. We will only retain the following main ideas.

One considers the second-order spectral tensor defined by relation (6.6). The integral lengthscales $L_u$ and $L_v$ are associated with integrals of the normal components $\hat{U}_{11}$ and $\hat{U}_{22}$ in the plane $k_1 = 0$:

$$\left.\begin{aligned} L_u &= \pi \frac{\int_{R^2} \hat{U}_{11}(k_1 = 0, k_2, k_3)\, \mathrm{d}k_2\, \mathrm{d}k_3}{\int_{R^3} \hat{U}_{11}(\boldsymbol{k})\, \mathrm{d}\boldsymbol{k}}, \\ L_v &= \pi \frac{\int_{R^2} \hat{U}_{22}(k_1 = 0, k_2, k_3)\, \mathrm{d}k_2\, \mathrm{d}k_3}{\int_{R^3} \hat{U}_{22}(\boldsymbol{k})\, \mathrm{d}\boldsymbol{k}}. \end{aligned}\right\} \tag{7.1}$$

It appears convenient to consider $\hat{\boldsymbol{U}}(\boldsymbol{k})$ through its eigenmodes, denoted $\phi_1$ and $\phi_2$, in an orthonormal frame $(\boldsymbol{e}^1, \boldsymbol{e}^2)$ lying in the plane normal to $\boldsymbol{k}$ (Herring–Craya representation), so that $\boldsymbol{e}^1$ lies in the plane normal to $\boldsymbol{\Omega}$. This representation is sketched in figure 24 for a wave vector normal to $\boldsymbol{\Omega}$:
$\phi_1$, which lies in the plane normal to $\boldsymbol{\Omega}$, will be called the two-dimensional mode† and $\phi_2$, the parallel mode. In the plane $\theta = \frac{1}{2}\pi$, the spectral tensor $\hat{\boldsymbol{U}}(\boldsymbol{k}, t)$ can be written in the axisymmetric form:

$$\hat{U}_{ij}(k, \theta = \tfrac{1}{2}\pi, t) = \phi_2(k, \tfrac{1}{2}\pi, t)\, P_{ij}(\boldsymbol{k}) + (\phi_1(k, \tfrac{1}{2}\pi, t) - \phi_2(k, \tfrac{1}{2}\pi, t))\, P^{\perp}_{ij}(\boldsymbol{k}). \tag{7.2}$$

† In strictly two-dimensional turbulence, the spectral energy is only concentrated in the plane $\theta = \frac{1}{2}\pi$, and $\phi_2$ disappears: $\phi_1 = \delta(k_1) E(k)/2\pi k$, $\phi_2 = 0$.

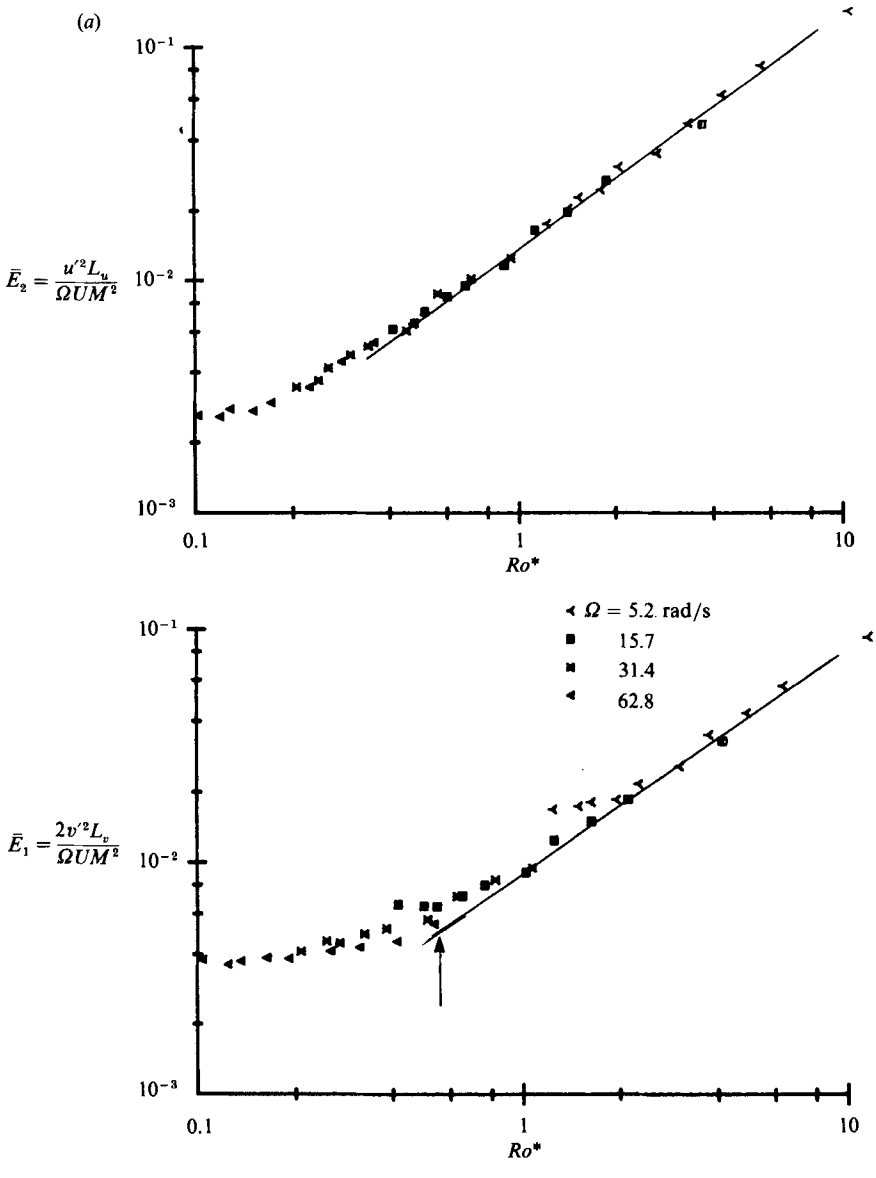


FIGURE 25(*a*). For caption see page 45.

For $0 < \theta < \frac{1}{2}\pi$, a more complicated form is obtained which takes into account the rotation of the principal axes of $\hat{U}_{ij}(\boldsymbol{k})$ (see Cambon & Jacquin 1989).

$$P_{ij}(\boldsymbol{k}) = \delta_{ij} - \frac{k_i k_j}{k^2} \tag{7.3}$$

is the projector in the plane normal to $\boldsymbol{k}$, and $P^{\perp}_{ij} = e^1_i e^1_j$, the projector in the plane normal to $\boldsymbol{\Omega}$. The energy of the wave ($\boldsymbol{k}$) reads

$$e(\boldsymbol{k}) = \tfrac{1}{2}\hat{U}_{ii}(\boldsymbol{k}) = \tfrac{1}{2}(\phi_1 + \phi_2), \tag{7.4}$$

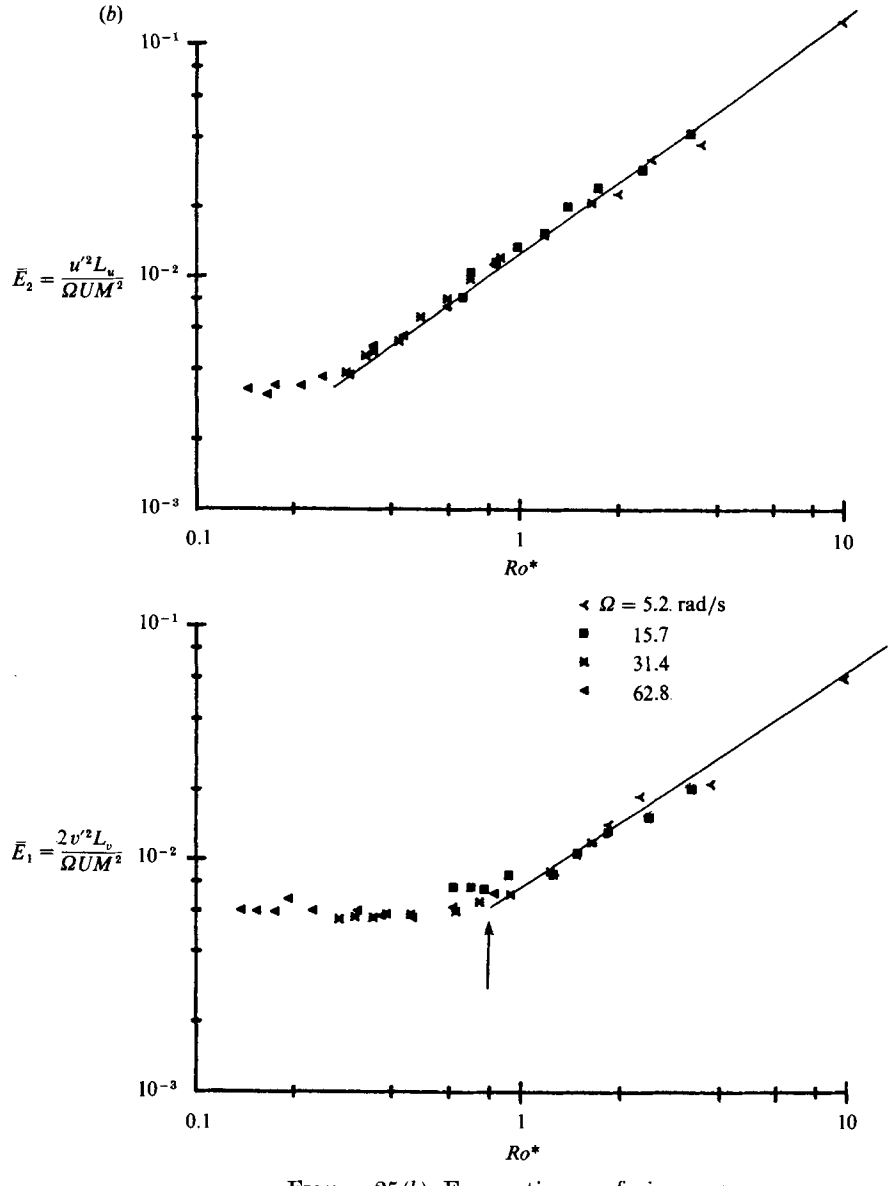


FIGURE 25(b). For caption see facing page.

and from the relations (7.1) and (7.2), the integral lengthscales can be written as follows:

$$\left.\begin{aligned} L_u(t) &= \frac{2\pi^2}{u'^2}\int_0^\infty k\,\mathrm{d}k\,\phi_2(k, k_1 = 0, t), \\ L_v(t) &= \frac{\pi^2}{v'^2}\int_0^\infty k\,\mathrm{d}k\,\phi_1(k, k_1 = 0, t). \end{aligned}\right\} \tag{7.5}$$

The experiment shows that when the macroscopic Rossby numbers are small enough, the lengthscales become very anisotropic with $L_v/L_u > 1$ (figure 9) whereas at the same time, the Reynolds stress structure is not very much affected (figure 7).

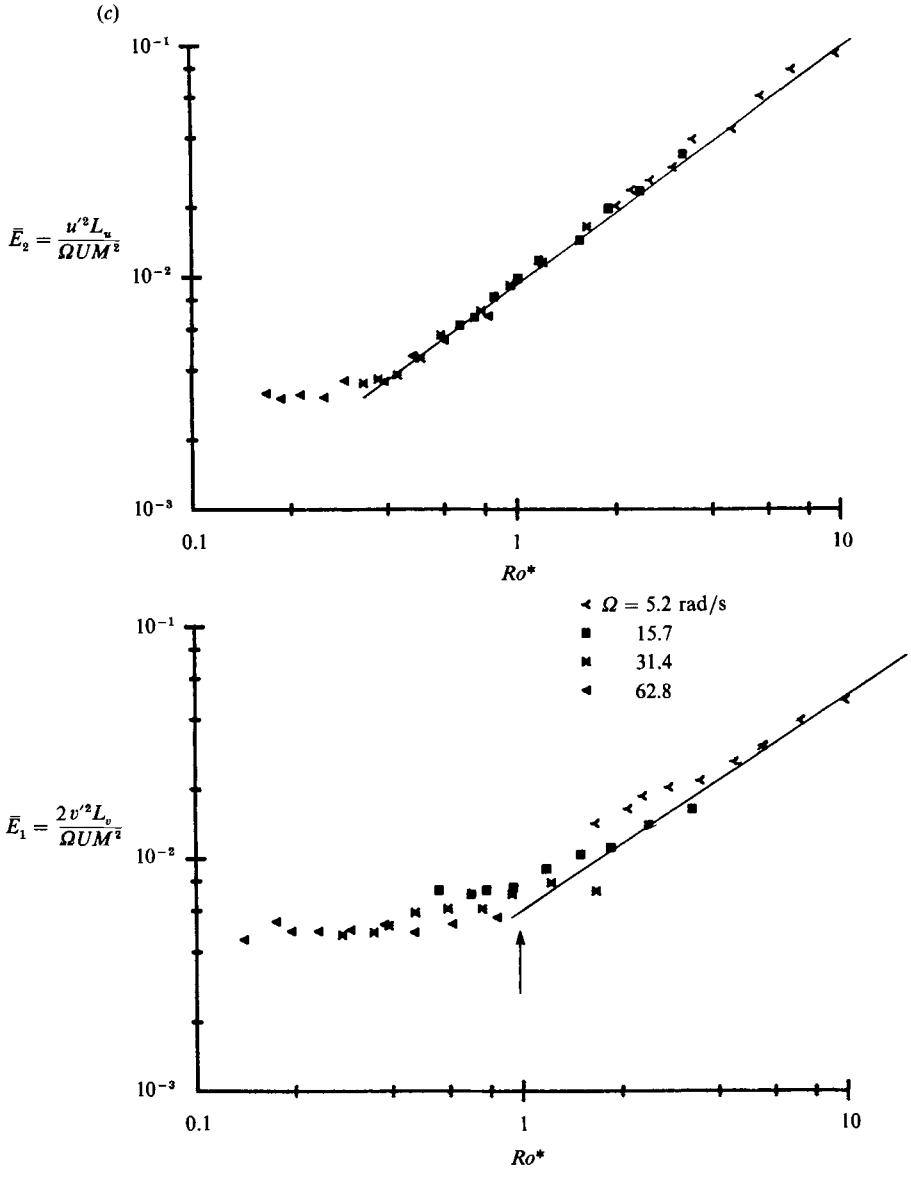


FIGURE 25. Components of the energy in the plane normal to $\boldsymbol{\Omega}$ versus the 'fictitious' Rossby number $Ro^*$: (*a*) $M = 10$ mm, (*b*) $M = 15$ mm, (*c*) $M = 20$ mm.

Relations (7.5) show that such trends are linked to a strong anisotropic structure of the second-order spectral tensor $\hat{\boldsymbol{U}}(\boldsymbol{k})$ in the plane $\theta = \frac{1}{2}\pi$, with $\phi_1 > \phi_2$.

Finally, the increase of the two-dimensional mode, $\phi_1$, can then be proposed as a possible manifestation of a transition towards two-dimensionality. This spectral interpretation of the transition from an isotropic three-dimensional turbulence towards a two-dimensional one, together with its connection with the behaviour of the lengthscales and the normal stresses, constituted one of the main contributions of Cambon & Jacquin (1989).

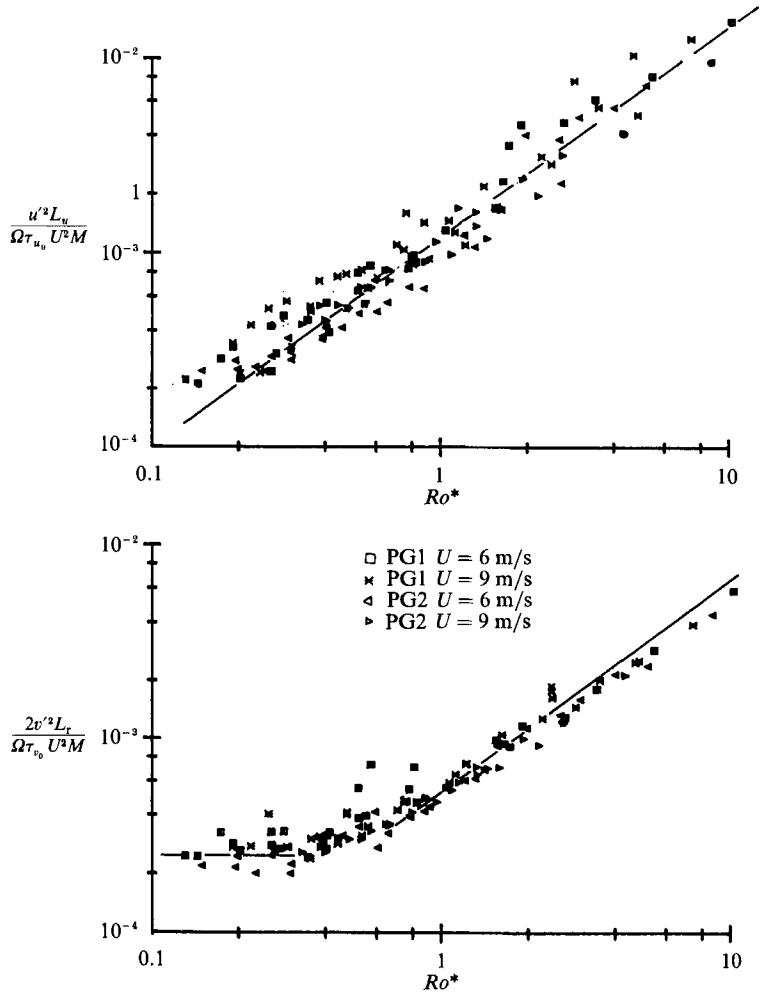


FIGURE 26. WN experiment: components of the energy in the plane normal to $\Omega$ versus the 'fictitious' Rossby numbers $Ro^*$ and $Ro^*$ for various configurations.

### 7.2. *Experimental characterization of the transition towards two-dimensionality*

With (7.5), $L_u$ and $L_v$ can be considered as an evaluation of the relative amount of energy in the plane $k_1 = 0$. Moreover, according to (7.5), the quantities

$$\left.\begin{aligned} E_2(t) &= u'^2 L_u(t) = 2\pi^2 \int_0^\infty k\,\mathrm{d}k\,\phi_2(k, k_1 = 0, t), \\ E_1(t) &= 2v'^2 L_v(t) = 2\pi^2 \int_0^\infty k\,\mathrm{d}k\,\phi_1(k, k_1 = 0, t), \end{aligned}\right\} \tag{7.6}$$

give the global contribution of each mode $\phi_1$ and $\phi_2$ in this plane. $E_1(t)$ and $E_2(t)$ can be defined as two components of the contribution of the equatorial plane to the total energy $q^2$. $E_1(t)$, which only involves the two-dimensional mode $\phi_1$, represents the strictly two-dimensional part of this energy.

Figure 25 shows $E_1$ and $E_2$ normalized by $\Omega U M^2$, versus the fictitious Rossby number $Ro^*$ for the three mesh sizes (the division of $E_1$ and $E_2$ by $\Omega$ is necessary to

correlate the results; $U$ and $M$ are then introduced, arbitrarily, for the normalization). One sees that for $Ro^* < 1$, the decay of $E_1$ is blocked whereas $E_2$ keeps on decaying for a time, the same way as during the quasi-isotropic regime $Ro^* > 1$. The arrows correspond to the 'transitional' values of $Ro^*$ already identified in §3.5. However, a blocking of $E_2$ is also observed in the lowest Rossby number range. In this situation, the total energy contained in the plane orthogonal to $\boldsymbol{\Omega}$ is conserved. This quantity reads:

$$\int e(k_1 = 0, k_2, k_3, t)\, \mathrm{d}k_2\, \mathrm{d}k_3 = \frac{1}{2\pi}\{E_1 + E_2\}(t). \tag{7.7}$$

Two different scenarios can be inferred concerning a possible asymptotic (very low Rossby number) two-dimensional flow: the first is that the whole energy (7.7) of the transverse waves is conserved, and the second, that only the two-dimensional mode $\phi_1$ is conserved. In physical space, both possibilities correspond to fluctuations normal to $\boldsymbol{\Omega}$. But in the second case no other movement is possible, whereas in the first case this two-dimensional random movement can be superimposed on a random solid body movement in the axial direction. The present experiment was unable to reach small enough values of the Rossby numbers to test the validity of these two possibilities.

Figure 26 shows the variation of the normalized $E_1$ and $E_2$ versus $Ro_u^*$ and $Ro_v^*$ obtained from WN for various configurations (the normalization adopted is that which gave the 'best' correlation; the time $\tau_{u0}$ or $\tau_{v0}$ are calculated from the integral lengthscales and the r.m.s. values measured in the initial section of the duct). The same trends are observed as in figure 25.

## 8. An interpretation of the effects of the mesh size of the grid

We have noted in figures 11 and 25 that when $M$ decreases, the transitional mechanisms of rotation were less pronounced and that the transition occurs at lower Rossby numbers (see arrows).

$M$ directly influences the Reynolds number of the flow and we propose here to show how the Reynolds number influence could explain the above-mentioned differences between various experiments.

A Reynolds-number effect could be expected in the following way: when the Reynolds number is small, i.e. for small grids, the inertial mechanisms of rotation responsible for the transitional mechanisms may be masked by pure viscous effects. The following analysis is proposed to check this possibility.

The peculiar role of the transverse waves ($\boldsymbol{k}$ normal to $\boldsymbol{\Omega}$) was underlined in the previous section. We consider the energy of these waves (see (6.14) and (7.4)), $e(k_1 = 0)$. In the presence of rotation, the equation for $e(k_1 = 0)$ retains the following classical form:

$$\left[\frac{\partial}{\partial t} + 2\nu k^2\right] e(k_1 = 0, k_2, k_3, t) = T(k_1 = 0, k_2, k_3, \Omega, t), \tag{8.1}$$

where

$$T(\boldsymbol{k}, t) = -Ik_1 \int_{\boldsymbol{p}+\boldsymbol{q}=\boldsymbol{k}} \langle \hat{u}_1(\boldsymbol{p}, t)\, \hat{u}_i(\boldsymbol{k}, t)\, \hat{u}_1(\boldsymbol{q}, t) \rangle\, \mathrm{d}\boldsymbol{q}, \tag{8.2}$$

represents a transfer function between the waves ($\boldsymbol{p}$), ($\boldsymbol{q}$) and ($\boldsymbol{k}$).

The present experiment has shown that a basic mechanism of rotation was to damp the inertial transfer $T(k_1 = 0, k_2, k_3, \Omega, t)$. The experiment also indicates that

the times $\tau_\Omega = (2\Omega)^{-1}$ and $\tau_v = 2L_v/v'$, whose ratio is $Ro_v$, are relevant to characterize these inertial mechanisms.

Concerning the viscous effects, they can be evaluated in the following way.

One considers the transverse waves of higher energy and characterizes them by the wavenumber

$$K = \frac{2\pi}{2L_v}. \tag{8.3}$$

In accordance with (8.1), the viscous damping of these waves can be characterized by the timescale

$$\tau_\nu = (2\nu K^2)^{-1}.$$

The ratio

$$E_v = \frac{\tau_\Omega}{\tau_\nu} = \pi^2 \frac{\nu}{\Omega L_v^2}, \tag{8.4}$$

defines an Ekman number which characterizes the relative influence of the inertial and viscous mechanisms in the balance equation (8.1).

A Reynolds number can then be introduced through the following relation:

$$E_v = 8\pi^2 \frac{Ro_v}{Re_v}, \tag{8.5}$$

with

$$Re_v = \frac{v'(2L_v)}{\nu}. \tag{8.6}$$

Figure 27 presents the different domains covered by the whole set of our experiments in terms of the three dimensionless parameters defined above. The straight lines correspond to relation (8.5). The corresponding values of the Reynolds number

$$Re = \frac{q\lambda}{\nu} \tag{8.7}$$

are also indicated for reference. They are calculated by means of the isotropic definition of $\lambda$:

$$\lambda = \left(\frac{10\nu q^2}{\epsilon}\right)^{\frac{1}{2}}. \tag{8.8}$$

The figure is interpreted as follows. When the Reynolds number is not large enough, a critical situation corresponding to $Ro_v < 1$ ($\tau_\Omega < \tau_v$) and $E_v \geqslant 1$ ($\tau_\Omega > \tau_\nu$) may occur. In this situation the inertial effects of rotation may be reduced by viscous effects. When the Reynolds number is sufficiently high and when the transitional mechanisms are triggered (say for $Ro_v \approx 1$), the Ekman number $E_v$ is sufficiently small and viscous effects on the transverse waves become negligible.

One sees in the figure that for the smaller mesh sizes the domains covered by the corresponding experiments approach the critical domain $Ro_v \leqslant 1, E_v \geqslant 1$.

The Reynolds numbers in the experiment of Wigeland & Nagib were much smaller than in our experiment ($Re_\lambda \lesssim 25$). The above argument may thus explain why the transitional mechanisms were less pronounced in the first experiment (see figures 17 and 26).

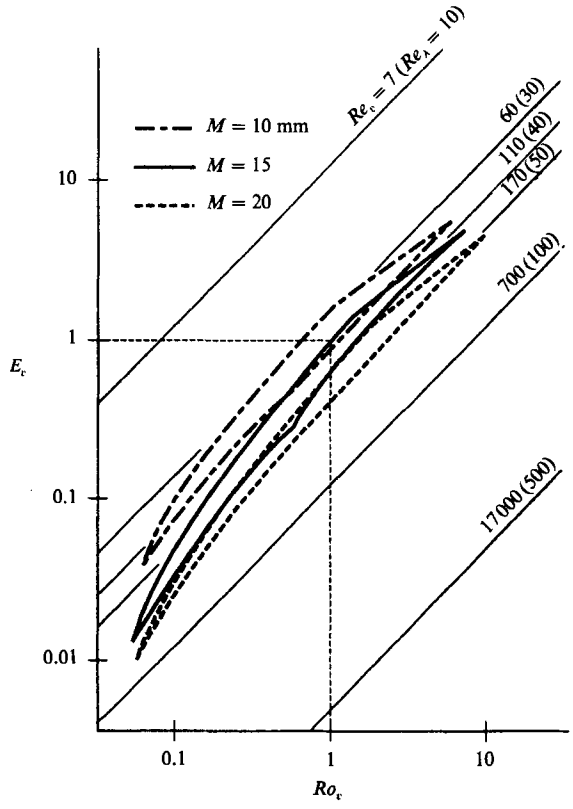


FIGURE 27. Parametric representation of the various experiments in terms of the transverse Ekman number $E_v$, Rossby number $Ro_v$ and Reynolds number $Re_v$.

## 9. Conclusions

The present experiment fulfils the various conditions of homogeneity: the mean flow is of solid-body rotation, the profiles of the second-order moments are regular in a large spanwise proportion of the duct and the Ekman dissipation is negligible.

It is confirmed that rotation slows the decay of turbulence (figure 4) and that it mainly affects the transversal part of the fluctuating field by strongly increasing the integral lengthscale $L_v$ (figure 9).

In contrast to the integral lengthscales, the structure of the Reynolds stress tensor is found to be little affected by rotation (figure 7).

One of the main contributions of the present study concerns the characterization of various regimes of the flow. The relevant parameters are the macroscopic Rossby numbers, $Ro_u$ and $Ro_v$, built separately on the axial and the normal components of the fluctuations. These parameters enable us to characterize a transition-like occurrence of the rotation dominated regime. The latter is associated with a stronger decrease of $Ro_v$ (figures 11 and 13).

A review of relevant theories helps to interpret various aspects of the experimental results.

First, a simple displaced-particle argument shows that a direct effect of the Coriolis force is the confinement of the transverse movements of the fluid particles. As a consequence, the mean transverse displacement of the fluid particles is limited to

$L_\Omega = v'/2\Omega$. The changes in the structure of the turbulent field, which occurs when $Ro_v < 1$, that is when $L_\Omega < 2L_v$, is thus associated with a consequence of this Coriolis constraint on the large eddies whose characteristic size is $2L_v$. This argument leads also to a simple physical interpretation of the anisotropy of the various integral lengthscales.

An extended analysis of the equations of motion was then performed, mainly through spectral analysis.

We first investigated the consequences of the linear wave regime on the statistics of the flow. We showed that, in contrast with the results of Ibbetson & Tritton, the interactions between the inertial waves and the boundaries of our apparatus are negligible. On the other hand, it was shown that the linear regime can strongly affect the structure of an initially anisotropic flow. This linear regime is less apparent in our experiment than in the experiment of Wigeland & Nagib.

Consequently, the anisotropic mechanisms brought to light in the experiment are primarily due to nonlinear mechanisms. As shown by Cambon & Jacquin (1989), the increase of the lengthscale ratio $L_v/L_u$ is related to a strengthening of the energy associated with the wave normal to the rotation axis, together with a predominance of the normal mode of the second-order spectral tensor associated to these waves. The contribution of this mode to the total kinetic energy (what we call the 'strictly two-dimensional part of the energy' in §7.2) can be evaluated through the quantity $v'^2 L_v$. The strong damping of the decay of this quantity (as soon as the Rossby number is small enough) brings an experimental confirmation of this transition mechanism (figure 25).

Finally, an interpretation of the effects of the mesh size of the grid is given in terms of Reynolds number influence. It is shown that for small Reynolds numbers (that is for small grid mesh sizes), the concentration of energy on the transverse waves occurring at small Rossby numbers can be counterbalanced by pure viscous dissipation (the latter is characterized by an Ekman number). A parametric representation of the experiments using a Rossby number, an Ekman number and a Reynolds number enables us to discriminate different regimes of the flow (figure 27).

The authors wish to thank P. Geffroy (ONERA) for his valuable contribution to the experiments. This work was supported in part by DRET under contract no. 87.001.57.

## REFERENCES

Aupoix, B., Cousteix, J. & Liandrat, J. 1983 Effects of rotation on isotropic turbulence. In *Turbulent Shear Flows 4* (ed. L. J. S. Bradbury, F. Durst, B. E. Launder, F. W. Schmidt & J. H. Whitelaw). Springer.

Batchelor, G. K. & Proudman, I. 1954 The effect of rapid distortion of a fluid in turbulent motion. *Q. J. Mech. Appl. Maths* **7**, 83–103.

Bardina, J., Ferziger, J. H. & Rogallo, R. S. 1985 Effect of rotation on isotropic turbulence: computation and modelling. *J. Fluid Mech.* **154**, 321–336.

Bertoglio, J. P. 1980 Influence des forces de Coriolis sur une turbulence soumise à des gradients. Thèse de Docteur Ingénieur, Université Claude Bernard, Lyon, février 1980.

Cambon, C. 1982 Étude spectrale d'un champ turbulent soumis à des effets couplés de déformation et de rotation imposés extérieurement. Thèse d'État, Université Lyon I.

Cambon, C. & Jacquin, L. 1987 Spectral analysis of a three dimensional homogeneous turbulence submitted to a solid body rotation. In *Advances in Turbulence 1* (ed. G. Comte-Bellot & J. Mathieu), pp. 170–175. Springer.

Cambon, C. & Jacquin, L. 1989 Spectral approach to non-isotropic turbulence subjected to rotation. *J. Fluid Mech.* **202**, 295–317.

COMTE-BELLOT, G. & CORRSIN, S. 1966 The use of a contraction to improve the isotropy of grid-generated turbulence. *J. Fluid Mech.* **25**, 657–682.

COMTE-BELLOT, G. & CORRSIN, S. 1971 Simple Eulerian time correlation of full and narrow-band velocity signal in grid generated 'isotropic' turbulence. *J. Fluid Mech.* **48**, 273–337.

COURSEAU, P. & LOISEAU, M. 1978 Contribution à l'analyse de la turbulence homogène anisotrope. *J. Méc.* **17**, 246–297.

CRAYA, A. 1958 Contribution à l'analyse de la turbulence associée à des vitesses moyennes. Publicatiöns Scientifiques et Techniques, Ministère de l'Air, France, no. 345.

DANG, K. & ROY, P. 1985 Direct and large eddy simulation of homogeneous turbulence submitted to solid body rotation. *Proc. of the 5th Symp. on Turbulent Shear Flows, Ithaca, NY.*

GENCE, J. N. & MATHIEU, J. 1979 On the application of successive plane strains to grid-generated turbulence. *J. Fluid Mech.* **93**, 501–513.

GREENSPAN, H. P. 1968 *The Theory of Rotating Fluids.* Cambridge University Press.

HOPFINGER, E. J., BROWAND, F. K. & GAGNE, Y. 1982 Turbulence and waves in a rotating tank. *J. Fluid Mech.* **125**, 505–534.

HUNT, J. C. R., STRETCH, D. D. & BRITTER, R. E. 1988 Length scales in stably stratified turbulent flows and their use in turbulence models. In *Stably Stratified Flow and Dense Gas Dispersion* (ed. J. S. Puttock), pp. 285–321. Clarendon.

IBBETSON, A. & TRITTON, D. J. 1975 Experiments on turbulence in a rotating fluid. *J. Fluid Mech.* **68**, 639–672.

ITSWEIRE, E., CHABERT, L. & GENCE, J. N. 1979 Action d'une rotation pure sur une turbulence homogène anisotrope. *C.R. Acad. Sci. Paris* **289** B, 197–201.

JACQUIN, L. 1987 Etude théorique et expérimentale de la turbulence homogène en rotation. Thèse d'Etat Université Lyon I octobre 1987.

JACQUIN, L., CAMBON, C. & MATHIEU, J. 1986 Analyse spectrale d'une turbulence homogène axisymétrique soumise à une rotation pure. *C.R. Acad. Sci. Paris* **302**, Ser. 2, no. 18, 1131–1134.

JACQUIN, L., GEFFROY, P. & LEUCHTER, O. 1988 Experimental study of rotation effects on grid generated turbulence for different mesh sizes. *2nd European Turbulence Conference, Berlin.* In *Advances in Turbulence 2* (ed. H. H. Fernholz & H. E. Fielder), pp. 167–174. Springer.

JACQUIN, L., LEUCHTER, O. & GEFFROY, P. 1989 Experimental study of homogeneous turbulence in the presence of rotation. In *Turbulent Shear Flows 6*, pp. 46–57. Springer.

JACQUIN, L., LEUCHTER, O. & GEFFROY, P. 1990 Etude expérimentale de la turbulence homogène en rotation. *La Recherche Aérospatiale* (in press).

LAKSHMINARAYANA, B. 1986 Turbulence modeling for complex shear flows. *AIAA J.* **24**, 1900–1917.

MORY, M. & CAPERAN, P. 1987 On the genesis of quasi-steady vortices in a rotating turbulent flow. *J. Fluid Mech.* **185**, 121–136.

PHILLIPS, O. M. 1963 Energy transfer in rotating fluids by reflection of inertial waves. *Phys. Fluids* **6** (4), 513–520.

ROGALLO, R. S. 1981 Numerical experiments in homogeneous turbulence. *NASA* TM-81315.

ROSE, W. G. 1966 Results of an attempt to generate a homogeneous turbulent shear flow. *J. Fluid Mech.* **25**, 97–120.

SPEZIALE, C. G., GATSTI, T. B. & MHUIRIS, N. M. G. 1989 A critical comparison of turbulence models for homogeneous shear flows in a rotating frame. In *Proc. Turbulent Shear Flows Symp., Stanford.*

TAVOULARIS, S. & CORRSIN, S. 1981 Experiments in nearly homogeneous turbulent shear flows with a uniform mean temperature gradient. *J. Fluid Mech.* **104**, 311–367.

TEISSÈDRE, C. & DANG, K. 1987 Anisotropic behaviour of rotating homogeneous turbulence by numerical simulation, AIAA Fluid and Plasma Dynamics Conference, Honolulu, Hawaii. *AIAA paper* 87-1250.

TOWNSEND, A. A. 1954 The uniform distortion of homogeneous turbulence. *Q. J. Mech. Appl. Maths* **7**, 706–727.

TOWNSEND, A. A. 1976 The structure of the turbulent shear flow, 2nd edn. Cambridge University Press.

TRAUGOTT, S. C. 1958 Influence of solid body rotation on screen produced turbulence. *NACA TN* 4135.

TRITTON, D. J. & DAVIES, P. A. 1981 *In Hydrodynamic instabilities and the transition to turbulence* (ed. H. L. Swinney & J. B. Gollub), pp. 229–240. Springer.

TRITTON, D. J. 1990 Some notes on shear flow turbulence in a rotating fluid. Submitted to the *J. Fluid Mech.*

WIGELAND, R. A. & NAGIB, H. M. 1978 Grid generated turbulence with and without rotation about the streamwise direction. *IIT Fluids & Heat Transfer Rep.* R. 78-1, Illinois Institute of Technology.